

Level 2 Photometric Calibration for the LSST Survey

Lynne Jones, Željko Ivezić, David Burke, Tim Axelrod
on behalf of The Photometric Calibration Team

ABSTRACT

This document describes the photometric calibration procedure for LSST Data Release catalogs. This procedure will use specialized hardware (an auxiliary telescope and narrow-band dome screen projector) to measure the wavelength dependence of the atmospheric and hardware response functions, together with a self-calibration procedure that leverages multiple observations of the same sources over many epochs, to deliver 1%-level photometry across the observed sky.

Contents

1	Introduction	2
2	Photometric Requirements	4
3	Overview of the photometric calibration process	6
3.1	Truth: From photons to counts	8
3.1.1	Normalized bandpass response, $\phi_b(\lambda)$	10
3.2	Model: How to calibrate counts	14
4	Details of the internal calibration process	19
4.1	Normalization of the hardware transmission	19
4.1.1	Generating the illumination correction	20
	Ghosting	21
	Pixel scale variation	23
	Non-uniformity in the Dome Screen Illumination and Stray/Scattered Light .	23
	The Total Illumination Correction	25

4.1.2	Error in the Normalization of the Hardware Transmission	26
4.2	Correcting for the Shape of the Hardware and Atmospheric Response Curve	26
4.2.1	Measuring the shape of the hardware response curve	29
	The narrow-band flat field illumination correction	31
	The expected effect of $\phi_b^{sys}(\lambda)$ variations	32
4.2.2	Measuring the shape of the atmospheric transmission curve	32
	Atmospheric absorption behavior	36
	Fitting the atmospheric absorption	37
	The expected effect of $\phi_b^{atm}(\lambda)$ variations	40
4.2.3	Errors in the shape of the hardware and atmospheric response	40
4.3	Normalization of the Atmospheric Transmission	41
4.3.1	Photometric vs. Non-photometric data	44
5	Fixing LSST to an external scale	44
5.1	Band to band (color)	45
5.2	Single bandpass to external flux system (absolute scale)	46
A	Filter Set	48
B	Areas for further investigation	48
C	Photometric measurements for non-main sequence stars	49
D	Glossary	50

1. Introduction

LSST is required to deliver 1%-level photometry across the observed sky and under a wide range of observing conditions (0.5%-level for repeat observations of the same source).

This represents about a factor of two improvement over the current state-of-the-art wide-field optical photometry delivered by SDSS under photometric conditions. This factor of two improvement will have a major impact on science deliverables because it implies that the error volume in the five-dimensional LSST color space will be over thirty times smaller than for SDSS-like photometry. This smaller error volume will improve source classification and the precision of quantities such as photometric redshifts for galaxies and photometric metallicity for stars. For example, a given spectral energy distribution (SED) corresponding to some galaxy type produces a line in the *ugrizy* multi-dimensional color space when redshifted, where the position of the galaxy along that line in *ugrizy* space is a function of redshift. Different galaxy SEDs produce lines that are often close to each other in *ugrizy* space and sometimes even cross. The smaller the error volume around an observed galaxy’s measured *ugrizy* colors, the smaller the number of different lines (thus, different SEDs) and different positions along the line (thus, different redshifts) which will be consistent with the measurement. The same conclusion is valid in the case of algorithms that estimate stellar effective temperature and metallicity, as well as any other model-based interpretation of measurements. Furthermore, the smaller error volume per source is advantageous even in the absence of any models. Two sources whose color differences produce a value of χ^2 per degree of freedom of 1, will have a χ^2 per degree of freedom of 4 when the errors are halved. In case of five degrees of freedom, $\chi^2 \text{ pdf} > 4$ will happen by chance in only 0.1% of all cases. Therefore, the ability to reliably detect color differences between sources is a strong function of photometric errors.

The factor of two reduction in photometric error results from two major differences between LSST and SDSS. First, each source will receive hundreds of observations over the ten years of the LSST survey. These series of repeat observations will be used to self-calibrate the photometric system across the sky and for each observation (akin, but not identical to, the uber-calibration procedure used by SDSS (Padmanabhan et al. 2008)), allowing LSST to operate in a wide variety of conditions. Secondly, the wavelength dependence of the hardware and atmospheric transmission response functions will be measured with auxiliary instrumentation on sufficiently fine angular and temporal scales to enable their explicit inclusion in the calibration procedure, rather than resorting to traditional approximations such as linear color terms. SNLS re-processing of CFHT Legacy Survey data found these color-dependent terms to be a significant contributor to the photometric calibration process (Regnault et al. 2009), on the level of a few to several percent.

This document describes the calibration requirements and processes for LSST Data Release photometry. At each Data Release, there will be a complete recalibration of all data acquired to that point, on approximately an annual schedule. These data products are referred to as Level 2 Data Products, in LSST Data Management terms. There will also be a

real-time data calibration process, based on the best available set of prior calibrated observations, to provide best-effort precision and accuracy for photometry for quality assurance, generation of alerts, and other quantities appropriate for nightly data generation (aka Level 1 Data Products). The Level 1 photometric calibration is not discussed here.

Section 2 reviews the survey requirements for photometric calibration, while Section 3 describes the philosophy behind LSST’s calibration procedure, first motivating this procedure by describing the true path of a photon through the atmosphere and LSST system and then from the calibration point of view, trying to recreate the transmission of those photons to the focal plane. Section 4 describes details of each step of the calibration procedure, including how each calibration measurement is obtained and applied to the science data along with expected errors originating from each step.

2. Photometric Requirements

The LSST Science Requirements Document (SRD) provides a set of requirements on the annual Data Release (Level 2) photometry based on measurements of bright, unresolved, isolated, non-variable objects from individual LSST visits. Bright implies that the measurement of the star’s brightness is not dominated by photon statistics, approximately 1-4 magnitudes fainter than the saturation limit in a given filter. Isolated implies that the star can be successfully de-blended from background galaxies and other stars. Non-variable objects are intrinsically not variable; these will be identified in an iterative fashion from the many epochs of LSST observations. The SRD specifications are:

1. **Repeatability:** the median value of the photometric scatter for each star (the rms of calibrated magnitude measurements around the mean calibrated magnitude) shall not exceed 5 millimags in *gri*, 7.5 millimags in *uzy* for bright, unresolved, isolated, non-variable objects. No more than 10% of these objects should have a photometric scatter larger than 15 mmag in *gri*, 22.5 mmag in *uzy*. This specifies the distribution of photometric errors (σ) and constrains both the repeatability of extracting counts from images and the ability to monitor (or model) the changes in the system response. It could be thought of as requiring the photometry of a single source to be consistent over time.
2. **Uniformity:** the rms of the internal photometric zeropoint error (for each visit) shall not exceed 10 millimags in *grizy*, 20 millimags in *uzy*, where the zeropoint for each visit is determined using bright, unresolved, isolated, non-variable sources. No more than 10% of these sources should be more than 15 mmag in *gri* or 22.5 mmag in *uzy* from the

mean internal zeropoint. This places a constraint on the stability of the photometric system across the sky as well as an upper limit on various systematic errors, such as any correlation of photometric calibration with varying stellar populations (or colors). This makes the photometry of many sources comparable over the entire sky, and when combined with the previous requirement, creates a stable photometric system across the sky and over time, in a single filter.

3. **Band-to-band photometric calibration:** The absolute band-to-band zeropoint calibration for main sequence stars must be known with an rms accuracy of 5 millimags for any color not involving u band, 10 millimags for colors constructed with u band photometry. This places an upper limit on the systematic error in the measurement of the system throughput as a function of wavelength. This requirement ties photometric measurements in different filters together, enabling precise measurement of colors.
4. **Absolute photometric calibration:** The LSST photometric system must transform to an external physical scale (*e.g.* AB mags) with an rms accuracy of 10 millimags. This requirement not only ties LSST internal photometry to photometry obtained from other telescopes, using other photometric systems, but also ties LSST internal photometry to a real physical scale. This places a constraint on the upper limit of the systematic error in the measurement of the total system throughput. This final step enables LSST photometry to be compared directly to data from other telescopes or to models (*e.g.* such as determining the albedo of an asteroid with a known diameter).

Requirements 1 and 2 must be met by measuring and then correcting for changes in hardware and atmospheric transmission as a function of time, location in the sky or focal plane, and result in a relative calibration within a single filter. Requirements 3 and 4 require comparison of LSST measurements to externally calibrated spectrophotometric standards, providing a relative calibration from filter to filter as well as an absolute physical scale for the overall system. Performance of the LSST system regarding requirement 1 can be verified by simply measuring the rms of the calibrated magnitude measurements. Verification of requirement 2 is more complicated; in a simulated system it is simple to compare the (simulated, thus known) true magnitudes of the stars to the best-fit magnitudes produced after calibration. In operations, this will be verified using a combination of simulations, comparisons to known standards, and evaluation of science outputs such as stellar locus diagrams. These last two tests are also relevant to verifying the final two requirements, 3 and 4.

3. Overview of the photometric calibration process

In traditional photometric calibration, a set of standard stars are observed at a range of airmasses to calculate zeropoint offsets and (typically) a single color-dependent extinction term per night. This is sufficient for photometry at the few percent level on photometric nights. However, historical weather data from Cerro Pachón tells us only 53% of the available observing time can be considered photometric even at the 1–2% level. To take advantage of the full 85% of the available observing time which is usable (total cloud extinction less than 1.5 magnitudes), and to reach the SRD specified requirements – 0.5% level photometric repeatability and 1% photometric uniformity – requires a new approach.

This new approach lies in splitting the measurement of the *normalization* of the throughput in each observation (the gray-scale zeropoint) from the *shape* of the throughput curve (the color dependent terms), and further, using separate procedures to measure the individual contributions of the telescope hardware response and the atmospheric throughput. The telescope hardware gray-scale zeropoint will be measured with a broadband flat field (detailed in section 4.1), while the hardware throughput response curve shape will be measured with narrow-band flat fields (detailed in section 4.2.1). The atmospheric gray-scale zeropoint will be calculated using the self-calibration procedure (detailed in section 4.3), while the atmospheric response curve shape will be measured with the auxiliary telescope (detailed in section 4.2.2). The separation of the normalization and shape of the throughput curve, as well as the separation of the telescope hardware from the atmospheric throughput, allows the use of methods optimized to measure the effect of each individual component of the system at the appropriate spatial and temporal scales, allowing us to achieve photometric calibration at the required levels.

A flowchart showing an overview of the steps from science observation to calibrated photometric measurements, together with the required calibration data products is shown in Figure 1. The *normalization* of the throughput will be corrected by using a flat field (for small spatial scale variations) and the self-calibration procedure (for larger spatial scale variations, as this is fundamentally limited by the spacing between calibration stars in each visit). The flat field can only correct for variations in the throughput of the hardware; the self-calibration procedure will primarily correct for variations in throughput due to atmospheric conditions (such as cloud extinction), although it can be extended to apply additional corrections for large spatial scale errors (illumination corrections) in the flat field. The *shape* of the throughput curve will be measured using both the narrow-band dome screen projector, to correct for variations in the shape of the hardware bandpass response across the field of view, and the auxiliary telescope, to correct for variations in the atmospheric absorption curve from visit to visit.

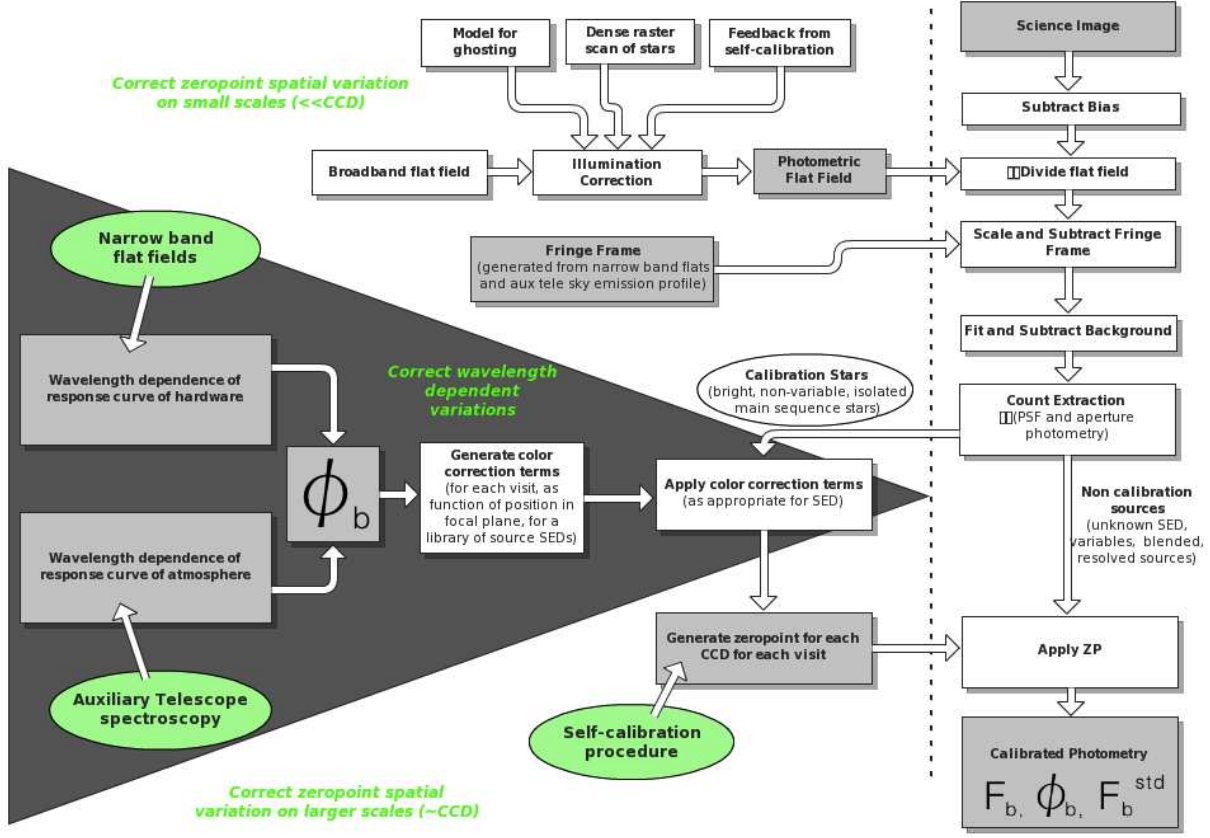


Fig. 1.—: **A flowchart of the Data Release photometric calibration process.** Everything to the left of the dashed line could be thought of as a calibration product, to be applied to data from each visit on the right of the dashed line. Each of the darker gray boxes indicates data or calibration products required to reach the final goal: calibrated photometric measurements. The light green circles point out significant LSST-specific calibration systems. The separation of the measurement and correction for wavelength dependent (shape) and wavelength independent (normalization) variations in the throughput can be seen in the three sections of the ‘calibration products’ on the left hand side. The upper portion, consisting mainly of flat-field effects, corrects primarily for small ($<<$ CCD) spatial scale gray-scale variations (although the illumination correction can also have larger spatial scale structure), the middle portion in the dark triangle corrects only for bandpass shape variations, while the bottom portion, consisting of the zeropoint corrections calculated from the self-calibration procedure, will only correct for larger spatial scale variations.

The rest of this section will provide a more in-depth overview of the calibration measurements required. We will start with a review of what is physically happening to photons in their path toward the focal plane (the ‘truth’), and then outline how LSST will translate the measured ADU counts back to photons above the atmosphere (the calibration ‘model’).

3.1. Truth: From photons to counts

Let us first consider how the photons from an astronomical object are converted into ADUs in the detector, paying attention to the various temporal or spatial scales for variability might arise in the LSST system to affect the final ADU counts (and ignoring errors in measurement, as this is the ‘truth’ of the flux transmission). This section is intended to motivate the separate measurement of the normalization and shape of the bandpass and introduce some important concepts, such as the normalized system response.

Given $F_\nu(\lambda, t)$ ¹ the specific flux of an astronomical object at the top of the atmosphere, at a position described by (alt, az) , the total flux from the object transmitted through the atmosphere to the telescope pupil is

$$F_\nu^{pupil}(\lambda, alt, az, t) = F_\nu(\lambda, t) S^{atm}(\lambda, alt, az, t), \quad (1)$$

where $S^{atm}(\lambda, alt, az)$ is the (dimensionless) probability that a photon of wavelength λ makes it through the atmosphere,

$$S^{atm}(\lambda, alt, az, t) = e^{-\tau^{atm}(\lambda, alt, az, t)}. \quad (2)$$

Here $\tau^{atm}(\lambda, alt, az)$ is the optical depth of the atmospheric layer at wavelength λ towards the position (alt, az) . Observational data (Stubbs et al. 2007a; Burke et al. 2010) show that the various atmospheric components which contribute to absorption (water vapor, aerosol scattering, Rayleigh scattering and molecular absorption) can lead to variations in $S^{atm}(\lambda, t)$ on the order of 10% per hour. Clouds represent an additional gray (non-wavelength dependent) contribution to τ^{atm} that can vary even more rapidly, on the order of 2–10% of the total extinction at 1° scales within minutes (Ivezić et al. 2007a).

¹Hereafter, the units for specific flux are Jansky ($1 \text{ Jy} = 10^{-23} \text{ erg cm}^{-2} \text{ s}^{-1} \text{ Hz}^{-1}$). The choice of F_ν vs. F_λ makes the flux conversion to the AB magnitude scale more transparent, and the choice of λ as the running variable is more convenient than the choice of ν . Note also, while $F_\nu(\lambda, t)$ (and other quantities that are functions of time) could vary more quickly than the standard LSST exposure time of 15s, it is assumed that all such quantities are averaged over that short exposure time, so that t refers to quantities that can vary from exposure to exposure.

Given the above $F_\nu^{pupil}(\lambda, alt, az, t)$, the total ADU counts transmitted from the object to a footprint within the field of view at (x, y) can be written as

$$C_b(alt, az, x, y, t) = C \int_0^\infty F_\nu^{pupil}(\lambda, alt, az, t) S_b^{sys}(\lambda, x, y, t) \lambda^{-1} d\lambda. \quad (3)$$

Here, $S_b^{sys}(\lambda, x, y, t)$ is the (dimensionless) probability that a photon will pass through the telescope's optical path to be converted into an ADU count, and includes the mirror reflectivity, lens transmission, filter transmision, and detector sensitivity. The term λ^{-1} comes from the conversion of energy per unit frequency into the number of photons per unit wavelength and b refers to a particular filter, *ugrizy*. The dimensional conversion constant C is

$$C = \frac{\pi D^2 \Delta t}{4gh} \quad (4)$$

where D is the effective primary mirror diameter, Δt is the exposure time, g is the gain of the readout electronics (number of photoelectrons per ADU count, a number greater than one), and h is the Planck constant. The wavelength-dependent variations in S_b^{sys} generally change quite slowly in time; over periods of months, the mirror reflectance and filter transmission will degrade as their coatings age. A more rapidly time-varying wavelength-dependent change in detector sensitivity (particularly at very red wavelengths in the y band) results from temperature changes in the detector, but only on scales equivalent to a CCD or larger. There will also be wavelength-dependent spatial variations in S_b^{sys} due to irregularities in the filter material; these are required by the camera specifications to vary (at a maximum) slowly from the center of the field of view to the outer edges, equivalent to a bandpass shift on the order of 1-2% of the effective wavelength of the filter. Wavelength-independent (gray-scale) variations in S_b^{sys} can occur more rapidly, on timescales of a day for variations caused by dust particles on the filter or dewar window, and on spatial scales ranging from the amplifier level, arising from gain changes between amplifiers, down to the pixel level, in the case of pixel-to-pixel detector sensitivity variations.

From equation 3 and the paragraphs above, we can see that the generation of counts $C_b(alt, az, x, y, t)$ from photons is imprinted with many different effects, each with different variability scales over time, space, and wavelength. In particular the wavelength-dependent variability (bandpass shape) is typically much slower in time and space than the gray-scale variations (bandpass normalization). These different scales of variability motivate us to separate the measurement of the normalization of S_b^{sys} and S^{atm} from the measurement of the wavelength-dependent shape of the bandpass.

3.1.1. Normalized bandpass response, $\phi_b(\lambda)$

This then leads us to introduce a ‘normalized bandpass response function’, $\phi_b^{obs}(\lambda, t)$, that represents the true bandpass response shape for each observation,

$$\phi_b^{obs}(\lambda, t) = \frac{S^{atm}(\lambda, alt, az, t) S_b^{sys}(\lambda, x, y, t) \lambda^{-1}}{\int_0^\infty S^{atm}(\lambda, alt, az, t) S_b^{sys}(\lambda, x, y, t) \lambda^{-1} d\lambda}. \quad (5)$$

Note that ϕ_b only represents *shape* information about the bandpass, as by definition

$$\int_0^\infty \phi_b(\lambda) d\lambda = 1. \quad (6)$$

Using $\phi_b^{obs}(\lambda, t)$ we can represent the (true, total) in-band flux of an object for each observation as

$$F_b^{obs}(t) = \int_0^\infty F_\nu(\lambda, t) \phi_b^{obs}(\lambda, t) d\lambda, \quad (7)$$

where the normalization of $F_b(t)$ corresponds to the top of the atmosphere. Unless $F_\nu(\lambda, t)$ is a flat ($F_\nu(\lambda) = \text{constant}$) SED, F_b^{obs} will vary with changes in $\phi_b^{obs}(\lambda, t)$ due simply to changes in the bandpass shape, such as changes with position in the focal plane or differing atmospheric absorption characteristics, *even if the source is non-variable*.

To provide a reported $F_b^{std}(t)$ which is constant for non-variable sources, we also introduce the ‘standardized bandpass response function’, $\phi_b^{std}(\lambda)$, a curve that will be defined before the start of LSST operations (most likely during commissioning). $\phi_b^{std}(\lambda)$ represents a typical hardware and atmospheric transmission curve, minimizing the difference between $\phi_b^{obs}(\lambda, t)$ and the standardized reported bandpass. Now,

$$F_b^{std}(t) = \int_0^\infty F_\nu(\lambda, t) \phi_b^{std}(\lambda) d\lambda, \quad (8)$$

is a constant value for non-variable sources.

Magnitudes provide an easy way to conceptualize the relationship between F_b^{obs} and F_b^{std} , provided that we define a ‘natural magnitude’

$$m_b^{nat} = -2.5 \log_{10} \frac{F_b^{obs}}{F_{AB}} \quad (9)$$

where $F_{AB} = 3631$ Jy. The natural magnitude, like F_b^{obs} will vary from observation to observation as $\phi_b^{obs}(\lambda, t)$ changes, even if the source itself is non-variable. The natural magnitude can be translated to a ‘standard magnitude’, m_b^{std} , as follows:

$$m_b^{nat} = -2.5 \log_{10} \frac{F_b^{obs}}{F_{AB}} \quad (10)$$

$$= -2.5 \log_{10} \frac{\int_0^\infty F_\nu(\lambda, t) \phi_b^{obs}(\lambda, t) d\lambda}{F_{AB}} \quad (11)$$

$$= -2.5 \log_{10} \left(\frac{\int_0^\infty F_\nu(\lambda, t) \phi_b^{obs}(\lambda, t) d\lambda}{\int_0^\infty F_\nu(\lambda, t) \phi_b^{std}(\lambda, t) d\lambda} \right) \left(\frac{\int_0^\infty F_\nu(\lambda, t) \phi_b^{std}(\lambda, t) d\lambda}{F_{AB}} \right) \quad (12)$$

$$m_b^{nat} = \Delta m_b^{obs} + m_b^{std} \quad (13)$$

where Δm_b^{obs} varies with the *shape* of the source spectrum, $f_\nu(\lambda, t)$ and the *shape* of the bandpass $\phi_b^{obs}(\lambda, t)$ in each observation. Note that $\Delta m_b^{obs} = 0$ for flat (constant) SEDs, as the integral of $\phi_b(\lambda)$ is always one. For non-variable sources, m_b^{std} will be non-variable as it represents the throughput in a standardized bandpass, $\phi_b^{std}(\lambda)$.

The natural and standard magnitudes can be tied back to the counts produced by the system by adding the correct zeropoint offsets. As Δm_b^{obs} removes all wavelength dependent variations in m_b^{std} ,

$$m_b^{std} = -2.5 \log_{10}(C_b^{obs}) + \Delta m_b^{obs} + Z_b^{obs} \quad (14)$$

the zeropoint correction here, Z_b^{obs} , contains only gray-scale *normalization* effects, such as variations due to the flat field or cloud extinction.

Examples of the Δm_b^{obs} due to variations in the shape of the hardware and atmospheric response curves are shown in Figure 2 and Table 1. Two main sequence stellar models (Kurucz 1993) – one with temperature 35000K (blue) and one 6000K (red) – were combined with three different atmospheric response curves (with airmass X=1.0 with minimal H₂O vapor, X=1.2 with a nominal amount of H₂O (the ‘standard’), and X=1.8 with a large H₂O vapor content) and two different hardware response curves (one ‘standard’ and one shifted in wavelength by 1%) to illustrate the resulting changes in observed natural magnitudes. In Figure 3, the X = 1.8 atmospheric response is combined with a 1% shift (the maximum allowed in the filter manufacturing specification from center to edge) in filter bandpass, thus altering the hardware response, for many main sequence Kurucz models spanning a range of *g* – *i* colors; the resulting changes in natural magnitudes are plotted. These examples demonstrate that the scatter in natural magnitudes induced by expected atmospheric and hardware transmission curve shape changes alone (without any gray-scale changes) can be larger than the SRD repeatability requirements would permit. Adding variations in the gray-scale normalization due to the hardware response and cloud extinction will increase the scatter in the observed magnitudes even further.

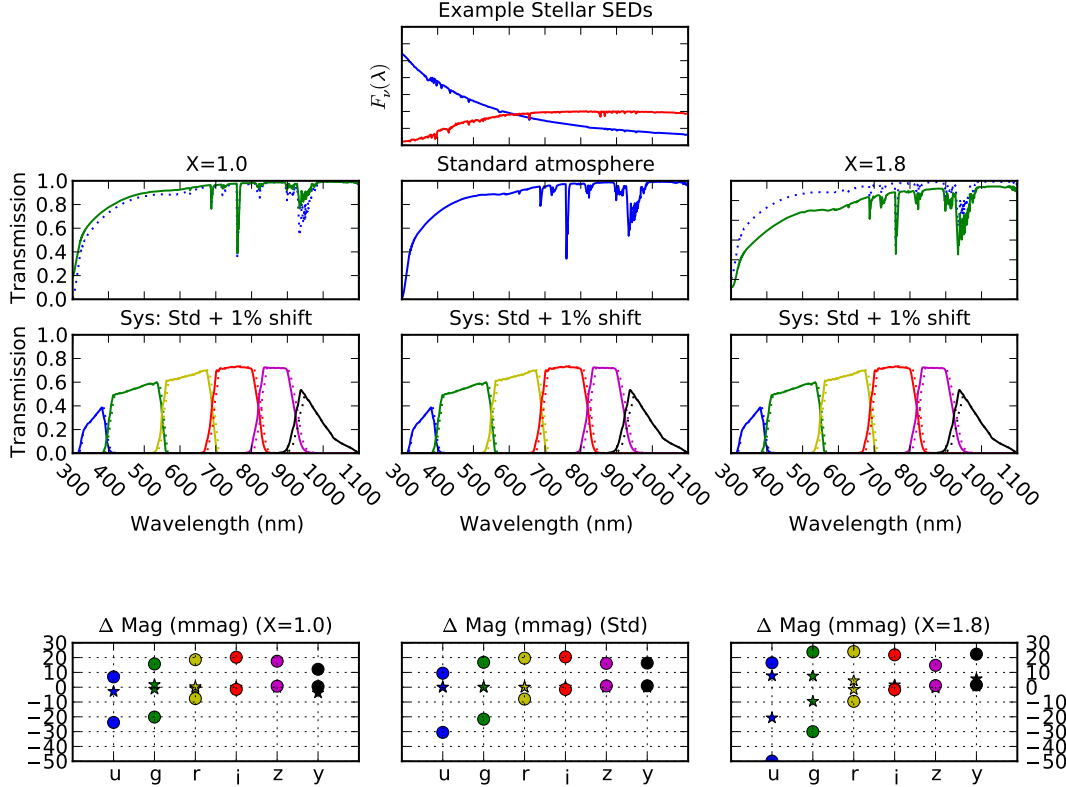


Fig. 2.—: Δm_b^{obs} due to variations in hardware and atmospheric bandpass shape. Two main sequence Kurucz model stars, one blue (35000 K, approximately O type) and one red (6000 K approximately G type), were used to generate natural magnitudes (see Eqn 9) using three different atmospheric transmission profiles and two different hardware transmission profiles. The stellar flux profiles are shown in the top center panel, while the atmospheric transmission functions ($S^{atm}(\lambda)$) are shown across the second row and the two hardware transmission profiles ($S_b^{sys}(\lambda)$) are duplicated across the third row. The atmospheric transmission profiles correspond to an airmass $X=1.0$, 1.2 and 1.8 (from left to right), with variable atmospheric absorption components. The $X=1.0$ atmosphere is very similar but not identical to the current LSST default $X=1.2$ atmosphere throughput curve, which is used as ‘standard’ here. The hardware transmission profiles consist of a ‘standard’ profile (matching the LSST current expected values) and version where the filter throughputs have been shifted by 1% of the effective wavelength of each filter (consistent with the shift expected near the spatial edge of each filter). The final row demonstrates the changes in observed magnitudes produced by the $X=1.0$, ‘standard’ and $X=1.8$ atmospheres (left to right, respectively), combined with both the ‘standard’ hardware transmission (represented by the star points) and the +1% shifted hardware transmission (represented by the filled circles) for both the red and blue stars. The exact differences in magnitudes resulting from this calculation are listed in Table 1.

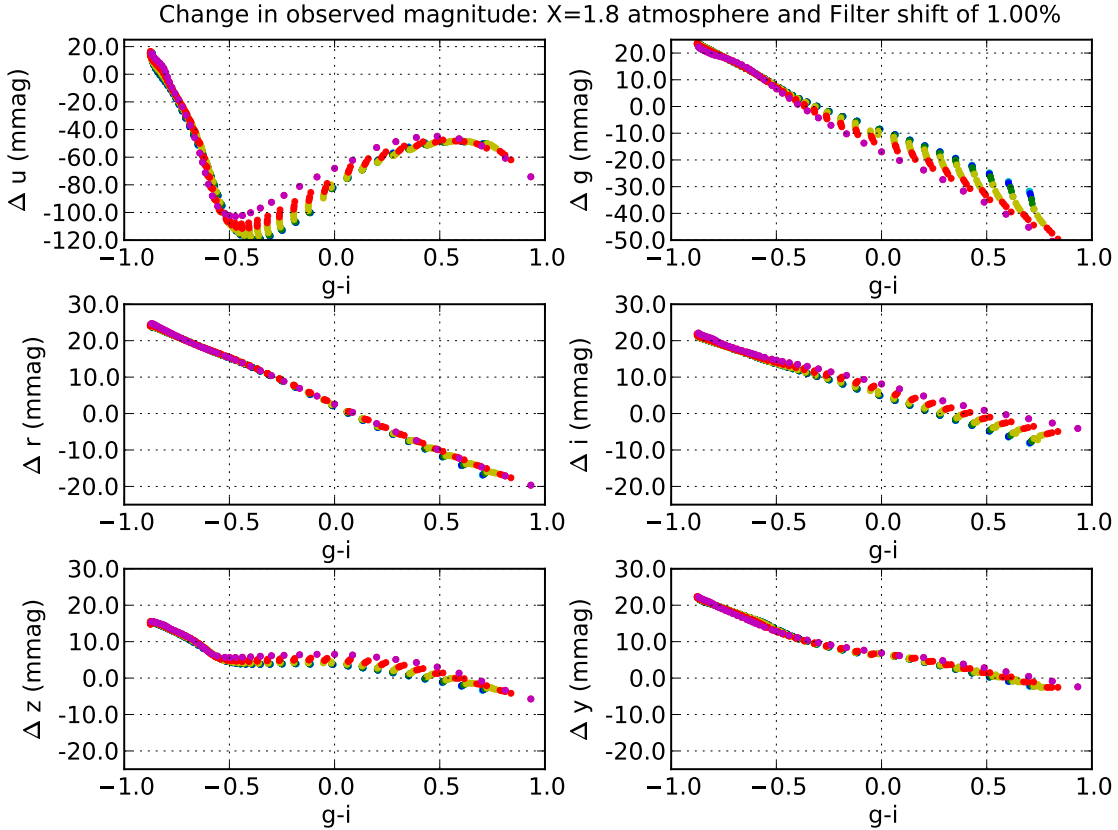


Fig. 3.—: Δm_b^{obs} due to a change in bandpass shape corresponding to a filter shift of 1% and an $X = 1.8$ atmosphere. 850 Kurucz models with temperatures between 5000K and 35000K and metallicity indexes between -5.0 and 1.0 (solar) were combined with a standard system response (standard atmosphere and standard hardware bandpasses), then with a total system response where the atmosphere was replaced by an $X=1.8$ atmosphere and the filter component of the hardware transmission was shifted by 1% (as in Fig 2). The points in each plot are color-coded by metallicity, in steps of 1 dex between -5.0 (blue) to 1.0 (magenta). It can be seen that the relationship between Δm_b^{obs} and $g - i$ can be parameterized, although generally not with a simple linear relationship. In some cases (such as seen in the Δu and Δg panels), calculating Δm_b^{obs} to SRD levels may require more than a simple $g - i$ color, but this is then primarily a function of metallicity (which is possible to determine given the $u - g$ color in addition to the $g - i$ information).

Table 1:: Δm_b^{obs} due to variations in system and atmospheric bandpass shape (see also Fig 2). The first two rows show the baseline ('standard') magnitude of the star. All other rows show the *change* in magnitude (in mmag) due to the variations listed at left. Any value larger than 5 mmag would be larger than the RMS scatter allowed by the SRD.

Bandpass	star	<i>u</i> (mag)	<i>g</i>	<i>r</i>	<i>i</i>	<i>z</i>	<i>y</i>
Standard (X=1.2) atm, std sys	red	21.472	20.378	20.000	19.911	19.913	19.913
Standard (X=1.2) atm, std sys	blue	19.102	19.503	20.000	20.378	20.672	20.886
		Δu (mmag)	Δg	Δr	Δi	Δz	Δy
Standard (X=1.2), +1% sys shift	red	-31	-22	-8	-2	1	1
Standard (X=1.2), +1% sys shift	blue	9	17	20	20	16	16
X=1.0, std sys	red	7	2	0	0	-0	-1
X=1.0, std sys	blue	-3	-1	-1	-0	1	-4
X=1.0, +1% sys shift	red	-24	-20	-8	-1	1	0
X=1.0, +1% sys shift	blue	7	16	19	20	18	12
X=1.8, std sys	red	-21	-10	-2	-0	0	1
X=1.8, std sys	blue	8	8	4	2	-1	6
X=1.8, +1% sys shift	red	-50	-30	-10	-2	1	2
X=1.8, +1% sys shift	blue	16	24	24	22	15	22

3.2. Model: How to calibrate counts

The previous section laid out the origins of ADU count variability from one observation to another. Now we will consider how we can, in practice, acquire the information necessary to convert a particular observed ADU count to a measurement of $F_\nu(\lambda, t)$ above the atmosphere for a particular object. In other words, how we can recreate the 'truth' by measuring and then compensating for the variations in $S^{atm}(\lambda, alt, az, t)$ and $S_b^{sys}(\lambda, x, y, t)$, using the separability of the normalization and shape of the total system response.

Let us first consider measurement of the variations in the hardware throughput curve, $S_b^{sys}(\lambda, x, y, t)$. As described in the previous section, these can be separated into wavelength-independent, normalization changes which can occur on short (nightly) timescales, and wavelength-dependent, shape changes which occur over a longer timescale. Examples of wavelength-independent changes include movement of dust particles on an optical surface or change in the gain of an amplifier channel. Examples of wavelength-dependent changes include the variations in the filter bandpass across the focal plane or deterioration of coatings on mirrors or lenses over time. We measure and correct for these variations in different ways.

We will measure the rapidly time variable gray-scale relative normalization changes in the hardware using standard broadband flat fields acquired at the start and end of each night through each filter, in a manner similar to traditional dome flats. This is discussed in detail in section 4.1. This calibration stage is particularly important for corrections on very small size scales, particularly on the pixel-to-pixel level. Later calibration stages depend on photometric measurements of stars using an aperture proportional to the Point Spread Function (PSF), and thus primarily contribute to calibration on scales larger than the PSF.

To measure the wavelength-dependent shape of the hardware response curve as a function of position in the focal plane, we will use a dome-screen system that is capable of producing light at a range of individual wavelengths - producing a data cube of ‘narrow-band flat fields’. At each x,y location in the focal plane, this data cube records $\phi_b^{sys}(\lambda, t)$. While this data cube of narrow-band flats could potentially be used as a ‘synthetic flat field’ by combining the individual narrow-band flats according to a chosen spectral energy distribution, generation of the entire data cube of narrow-band flats is too time-consuming to complete on a daily basis. Instead, the full narrow-band flat field scan will only be repeated on a time interval adequate for measurement of the more slowly variable $\phi_b^{sys}(\lambda, t)$, approximately monthly (but to be determined during commissioning). This measurement is discussed in detail in section 4.2.1.

It is important to consider that before these flat fields (both the broadband and the narrow-band flats) can be used to measure S_b^{sys} , they must be modified to correctly produce *photometrically* uniform measurements of stars of a defined reference SED across the field of view. This correction is called the ‘illumination correction’. The illumination correction must correct the observed flat fields for effects resulting from non-uniform illumination of the dome screen, for the effect of pixel scale variations across the field of view, for ghosting caused by internal reflections in the camera, and for the presence of stray or scattered light arriving in the focal plane on path that are not part of the optical design (such as light bouncing from the dome floor or glinting off a filter holder). See figures 5 and 6 for a visual example of the illumination correction and its importance to image processing. The illumination correction will be wavelength dependent; for the narrow-band flat fields, an illumination correction for each wavelength must be generated. The illumination correction (including ghost corrections) will be generated by combining measurements of bright, dense star fields rastered across the field of view during specialized observing sequences and further corrections generated by the self-calibration stage (discussed below in section 4.1). For the narrow-band flat fields, forward modeling will be useful in generating the illumination correction. This may include ZEMAX modeling, constrained with measurements from the ‘camera calibration optical bench’ (CCOB) and/or with measurements where the dome screen was illuminated in narrow-band mode at a single location only. Further corrections

will be generated by the self-calibration stage (discussed below in section 4.2.1). The illumination correction is expected to be stable with time and will be remeasured only when the optical path of the telescope is altered.

Next, considering $S^{atm}(\lambda, alt, az, t)$, we will again separate the measurement of the shape of the atmospheric response and the measurement of normalization of the transmission. The currently available data is still incomplete, but suggests that the wavelength-dependent variations in $\phi^{atm}(\lambda, t)$ change smoothly over spatial scales larger than the field of view and over several minutes. By using an auxiliary telescope equipped with a spectroscope to observe bright stars with known SEDs, we can measure atmospheric absorption at a variety of positions in the sky every 5–10 minutes throughout the night. These observations are used as constraints for MODTRAN atmospheric models, generating representations of the atmospheric throughput in the form of a set of absorption components as a function of alt, az, t . These components can be interpolated in time and space to generate a wavelength-dependent atmospheric absorption profile, $\phi_b^{atm}(\lambda, alt, az, t)$, for each observation. This process is discussed in detail in section 4.2.2.

In order to correct for the more rapid gray-scale variations in the relative normalization of $S^{atm}(alt, az, t)$ due to cloud extinction, we must use the observations of stars in the images themselves, as SDSS observations suggest that cloud extinction can vary by 0.01 magnitudes on the scale of a CCD (Ivezić et al. 2007a) on timescales as fast as a few minutes. This ‘self-calibration’ procedure could be thought of as creating a massive calibration ‘standard’ star catalog, where the calibration stars are all of the non-variable, main-sequence stars in the science images; the main difference is that the true magnitudes of the calibration stars have to be bootstrapped from the many different observations of the survey. For every main sequence star identified as non-variable, isolated, and in the desired (bright) magnitude range, corrections for the broadband flat field and $\phi_b^{sys+atm}(\lambda, t)$ must be applied to produce a standardized magnitude, m_b^{std} , then in the self-calibration procedure we minimize the difference between the standardized magnitude and a model magnitude,

$$\chi^2 = \sum_{ij} \left(\frac{m_{b,ij}^{std} - m_{b,ij}^{model}}{\sigma_{b,ij}^{std}} \right)^2 \quad (15)$$

where the model magnitude is derived from the best-fit ‘true’ magnitude of the calibration star and a model describing how we expect the magnitude to vary from observation to observation. In the simplest self-calibration plan, this model simply consists of a normalization constant (zeropoint offset) for a ‘patch’ equivalent to the size of a CCD,

$$m_{b,ij}^{model} = m_{b,i}^{best} - \delta z_{b,j}. \quad (16)$$

This produces best-fit magnitudes for the calibration star catalog as well as zeropoint off-

sets (normalization constants) for each CCD in every observation, allowing us to correct for atmospheric extinction on the scale of a CCD. By adopting a more complex model, this procedure can also correct for variations in the relative normalization of the total system throughput beyond those contributed by cloud extinction (such as remaining errors in the illumination correction for the broadband and narrow-band flat fields), but is generally limited by the number of stars and number of observations of each star that are obtained. A CCD size patch provides about 100 stars per patch, allowing good signal to noise when determining cloud extinction which varies from observation to observation. Using this self-calibration procedure, It may be possible to determine longer term effects (such as the illumination correction) down to scales approximately equivalent to the PSF. This is similar in nature to the ubercal method applied to SDSS in Padmanabhan et al. (2008), and is discussed in more detail in section 4.3.

Repeating Equation 14 above, adjusting *obs* indexes to *meas* to reflect the difference between the true and measured quantities,

$$m_b^{std} = -2.5 \log_{10}(C_b^{meas}) + \Delta m_b^{meas} + Z_b^{meas} \quad (17)$$

we can relate the terms in this equation to the corrections just described above. Δm_b^{meas} originates from the difference between $\phi_b^{meas}(\lambda, t, x, y)$ and $\phi_b^{std}(\lambda)$ convolved with the source SED, and thus it depends on the shape of the total system response as well as the shape of the source SED. Δm_b^{meas} will be calculated by combining a series of model SEDs with $\phi_b^{meas}(\lambda, t, x, y)$ at various locations in the focal plane, creating a lookup table of values to apply to measured magnitudes. For many sources (but not calibration stars), LSST will simply assume that the source has a flat SED, at which point the Δm_b^{meas} values become zero, although users may create their own SED and correction tables based on their knowledge of the true SED (see Appendix C). The Z_b^{meas} zeropoint offset comes from any normalization constants generated by the self-calibration procedure (in the simple model, just the $\delta z_{b,j}$ in equation 16 above).

These standard magnitudes are calibrated for variations in the observed bandpass shape (where applicable) and relative normalization, thus are directly comparable from one observation to the next. However, they are not yet tied to an external physical scale or from one filter band to another, and thus only define an internally calibrated LSST magnitude in a particular filter.

To fulfill SRD requirements 3 and 4, these internally calibrated natural magnitudes must also be tied from one filter band to another, and then tied to an absolute external physical scale. For this, a further set of measurements is needed. In all filters, a set of spectrophotometric standards must be observed, and calibrated using the steps described above. Then the known SED is combined with the standard bandpass shape to generate

synthetic color photometry. The synthetic colors are then compared with the calibrated measured standard magnitudes to calculate Δ_{b-r} , the corrections needed to tie measurements in each filter together (referenced to r band). At this point, only one final measurement is necessary to tie the entire system to an external physical scale: an r band LSST natural magnitude measurement of an absolutely calibrated source on a photometric night. Although in theory these last two steps could be done with a single externally calibrated object, on a single photometric night, a larger set of external reference objects with well known AB magnitudes will be used to reduce systematic errors. This defines an AB magnitude,

$$m_b^{AB} = m_b^{std} + \Delta_{b-r} + \Delta_r \quad (18)$$

which can be compared to absolute physical flux scales.

The sequence for photometric calibration is then:

1. Acquire a broadband flat in each filter at the start and end of each observing night. Generate a full, wavelength-dependent illumination correction for the flats on a much longer time interval (timescale to be determined, but much longer than monthly). Apply the appropriate illumination correction to the broadband flat. Apply flat field to images directly.
2. After remaining image processing (bias correction, fringe correction, etc) extract ADU counts of sources from images.
3. Acquire the data cube of narrow-band flat field images, approximately monthly. Apply wavelength-dependent illumination correction. Measure $\phi_b^{sys}(\lambda, t, x, y)$.
4. Acquire spectra of known stars roughly every 5–10 minutes throughout each night, fit for atmospheric absorption coefficients and generate $\phi_b^{atm}(\lambda, t)$ for each science images.
5. Combine ϕ_b^{atm} and ϕ_b^{sys} with a range of model SEDs to create lookup tables for Δm_b^{meas} for various locations in the focal plane.
6. At appropriate intervals (such as at Data Releases), run the self-calibration procedure, applying Δm_b^{meas} to stars chosen for self-calibration procedure and minimizing χ^2 from equation 15.
7. Apply appropriate Z_b^{meas} (and potentially Δm_b^{meas} values) to all objects in Data Release catalog, producing standardized magnitudes.
8. Apply measured corrections Δ_{b-r} and Δ_r , producing absolutely calibrated magnitudes.

This results in calibrated m_b^{AB} values in a standardized bandpass shape, with above-the-atmosphere fluxes.

4. Details of the internal calibration process

The next subsections expand on each of the photometric calibration steps leading to natural magnitude and standard magnitude measurements described above, including how each correction is measured, calculated and applied. The steps described in this section are applied to each filter independently. The end result of the internal calibration process is a record of m_b^{nat} and $\phi_b^{sys+atm}(\lambda)$ (or the parameters which allow reconstruction of $\phi_b^{sys+atm}(\lambda)$) measured for each object in each observation. In addition, there will be a reported spectral energy distribution (SED) assumed for each object ($f_\nu(\lambda)$) and an associated m_b^{std} that is the natural magnitude corrected for variations in the bandpass shape. In cases where the assumed SED is flat, m_b^{std} will be equal to m_b^{nat} .

4.1. Normalization of the hardware transmission

Compensation for variations (in x, y, t) in the normalization of the hardware transmission (S_b^{sys}) will be done using a broadband flat field generated using a broad band source illuminating a specialized dome screen projector. This is the first step in photometric calibration and is necessary to correct for spatial variations in the normalization of S_b^{sys} that are smaller than a few times the PSF (and with the simple self-calibration model described above, is necessary to correct for any variations smaller than the scale of a CCD).

The dome screen projector is an array of projectors mounted in the dome of the LSST enclosure, specially designed to provide very uniform illumination to the LSST étendue (the incoming aperture of the telescope, taking into consideration the desired angle of the incoming light) while minimizing any light straying beyond the étendue. In addition, the dome screen will be able to project both broadband and tunable narrow-band (essentially monochromatic) light sources, providing both broadband (broadband) and narrow-band flat fielding capabilities. More details of the narrow-band flat field capabilities are provided in section 4.2.1. The dome projector system is different from a traditional dome screen in that the ‘screen’ is a series of light sources, rather than a screen reflecting a single light source.

For both broadband and narrow-band flat field flat fields, the projectors are designed to fill the LSST étendue with a uniform illumination smoothly varying by less than 1% across the camera focal plane (corresponding to less than 10% variability across the projector surface) and less than 0.25% on scales smaller than 0.5° (a little larger than the size of a CCD). The projectors will also be designed to limit the extent of light emitted outside the étendue seen by the camera to reduce stray light in the flat fields (Gressler et al. 2010). The broadband light source can be tuned to have any chosen spectral profile; this will be chosen

during commissioning. For simplicity in discussing the next few sections, let us assume that this is a flat $F_\nu(\lambda)$ profile.

Although the dome screen is engineered to illuminate the LSST étendue very uniformly on scales approximately the size of a CCD (the engineering requirement of less than 0.25% variability translates to an RMS variation of 0.7 mmag on these scales), the variability across the full focal plane will exceed LSST SRD requirements. However, even if the dome screen illumination were perfectly uniform and no stray or scattered light entered the telescope, the observed flat field still could not be applied directly to science images with the expectation of achieving photometric uniformity in measurements of stellar sources, due to the presence of ghost images in the observed flat field and the effect of plate scale variation from the center to the edge of the field of view. The correction which must be applied to the observed flat to produce the desired photometrically correct flat is called the ‘illumination correction’.

4.1.1. Generating the illumination correction

To produce a truly ideal photometric flat field for measuring stellar sources, we would ideally start with a point source of known illumination, at infinity, extending over an infinitesimally small angular patch of sky and emitting uniformly in all directions as a Lambertian object, then move this point source to all locations within the telescope field of view – essentially, observing a controllable ‘star’ at all positions in the focal plane, with no atmosphere. In addition, this point source would emit the same spectral energy distribution (SED) as the source we wish to measure. We would then raster this point source over the telescope field of view in steps of a pixel’s angular size, and at each location measure the counts within a fixed aperture centered on the central ray from those coordinates. After normalizing the measured array of intensities to unity, the resulting data can be viewed as an image – the ‘ideal photometric flat’ for the selected SED. This would appear slightly different than a usual flat field image; *e.g.* dead pixels would not stand out, as they would be averaged into each aperture which overlapped them. When performing photometry, its use would be slightly different as well; instead of dividing the raw pixels by the flat, stellar photometry would consist of doing the aperture sum on the raw pixels and then dividing by the value of the photometric flat at the aperture center. The resulting magnitudes for stars (of the selected SED) measured with this technique would be indeed be uniform across the entire field of view - this would be an ideal photometric flat field.

In practice, we do not have a point source of this nature to create this ideal photometric flat. (Note that raster scans of stars attempt to recreate this flat field, but suffer from limited angular resolution and variability in the atmospheric transmission during the sequence of

exposures, which limit the capabilities of these scans). Typical astronomical flat fields are generated from dome screens, the twilight sky or dark sky flats, all of which contain light sources that illuminate the entire telescope field of view simultaneously. These sources are also only approximately Lambertian, as they do not emit light uniformly over all angles, and are only approximately uniform over the field of view. In addition, each has an SED which differs from that of the source to be measured. Each of these differences contributes toward the necessity of the ‘illumination correction’, the correction we must apply to the observed flat field to produce a ‘photometric flat’ which produces uniform photometry across the focal plane.

For LSST, we will be using the dome screen projectors described above (section 4.1). Flat fields produced by observing the dome screen will (as typical) not create an photometric flat. While the dome screen projectors will be designed to be uniformly illuminated to 1% over the focal plane, this is already beyond the SRD specifications for photometric uniformity. There will be also light scattered within the camera dewar and some fraction of the light within the étendue will have undergone multiple reflections within the camera refractive optics (creating ‘ghost’ images of the light from the dome screen). Estimates by Photon Engineering, Inc. (Tucson, AZ) indicate that $\approx 1 - 2\%$ of the light that reaches the camera focal plane may be stray light that did not originate within the LSST étendue. In addition, projection effects associated with the telescope optics will cause a variation in the pixel scale from the center to the outer edges of the field of view on the order of a few percent (very typical of telescopes with large fields of view), so that the pixels near the center of the field subtend a larger area and gather more light from the dome screen. All of these effects must be removed from the observed flat field by the illumination correction; we will define the illumination correction to be the ratio between the observed flat field and the desired photometrically uniform flat field.

Ghosting

With complex optical systems (such as the LSST camera), reflections from each of the surfaces in the optics can cause light to be diverted from its primary path, resulting in an ‘optical cross-talk’ where light received in one pixel in the focal plane contains contributions from illumination sources that could be widely separated from the central ray which would project onto that pixel. The ghost images that are produced by this process are easy to identify when a single point source is in the field of view, but when the entire field of view is illuminated, it is not possible to separate the light in a pixel that is the result of ghosting from the light in a pixel that has been received directly from the source.

In the LSST system, we expect the primary sources of ghosting to be reflections from the

surface of the detector onto the back surface of lens 3, between the back and front surfaces of the filter, and from the surface of the detector and the front side of lens 3. In general, the ghosts produced by reflections between lens 3 and the detector are expected to have an amplitude $\approx 5 \times 10^{-4}$ relative to the flux of the source. The ghosts due to filter reflections become especially prominent at wavelengths where the filter transmission approaches 50%. Tests with the Pan-STARRS narrow-band flat field system (Stubbs et al. 2010) show that at these wavelengths, the fraction of light in ghosts can reach about 15% of the total light in the focal plane. Other ghost images, due to reflections between lens surfaces, should contain about $\approx 10^{-5}$ times the flux of the source, although there can also be a special case of ghosting where the reflected light, due to the alignment of the optics, is focused into a ring in the focal plane – this special case is called the ‘pupil ghost’. While the location of most ghosts in the focal plane have a dependency on the position of the source in the image, the pupil ghost (because it is focused), does not and thus contains light from *every* source in the image, and thus can become a significant ghost, if the total light in the image (from sources and from background) is sufficiently large. The distribution of ghosts in the focal plane predicted from raytracing the LSST optical design (including the expected performance of the lens and filter coatings) from a single source is shown in Figure 4.

The distribution of ghost light creates in the focal plane is predictable and based on the optics configuration and coatings. The pattern (where the light from each ghost reflection arrives in the focal plane) is constant. However, the relative intensity of different ghost reflections will change depending on the wavelength of the incoming light. Thus, the final distribution of ghost light in the focal plane is wavelength dependent and will change with the SED of the source illumination.

Ghosting becomes a problem with the flat fields because every pixel contains light not only directly from the dome screen, but also light which has been reflected in the optics from other regions of the dome screen – and these are indistinguishable. The amount of ghosted light in a particular pixel depends on the details of the optical path, the amount of light coming each region of the dome screen, and the SED of the dome screen.

We can produce an initial correction to the observed flat field to removed ghost light by using a ZEMAX model of the optics (including the details of the optical coatings of each surface, including the filters), and by assuming that the dome screen is uniform and the SED is known. This initial correction will later be refined as part of the self-calibration process. The ZEMAX model will be constrained by observations of the optical system, which will come a combination of measurements from the Camera Calibration Optical Bench (CCOB) (see more information in the Glossary, Section D), in-laboratory measurements of the filter transmission as a function of radius, and by illuminating a single point in the array of dome

screen projectors (creating a semi-scannable, semi-Lambertian ‘star’ to create identifiable ghosts in the focal plane). The dome screen itself is of course not truly uniform, but a small non-uniformity (< 1%) combined with the fact that the ghost images are a small fraction of the direct light should reduce errors induced by this assumption to below the SRD limit. The SED of the light generated by the dome screen is well-controlled by the nature of the dome screen projectors.

Pixel scale variation

The pixel scale will vary from the center to the edge of the field of view due to projection effects in the optical system. As pixels in the center of the field of view then view a slightly larger solid angle than pixels near the edges, the number of photons captured from the dome screen (or the night sky background) in these pixels is slightly higher. For LSST, this variation is on the order of a few percent.

Although the light captured from the night sky background shows the same effect as the flat field, the total flux from astronomical sources is *unchanged* by the pixel scale change. The photons from a particular source may be spread over slightly more or slightly fewer pixels, but the total flux remains the same (note that magnitudes per arcsecond² do not act in the same manner, so extended sources must be handled with care). If the science images are divided by a flat field without correcting for the pixel scale change, the images will appear to have a uniform background, but the photometry from the stars will be incorrect (as the stars in the center would have been divided by a larger flat field value than the stars near the edge). The gradients in the flat field caused by pixel scale change must therefore be removed from the observed flat field in the illumination correction.

The observed flat field can be corrected for pixel scale variation by using the World Coordinate System (WCS) distortion map for the camera, obtained from observations of dense star clusters.

Non-uniformity in the Dome Screen Illumination and Stray/Scattered Light

The illumination from the dome screen could vary by up to 1% across the field of view. Stray light scattered from other unmodeled sources (such as light bouncing off the dome floor and back into the telescope optical path) could contribute 1-2% of the total light in the flat field, according to estimates from Photon Engineering, Inc. (Tucson, AZ). There may be systematic differences in exposure time across the field of view due to camera shutter movement. These effects are difficult to model accurately.

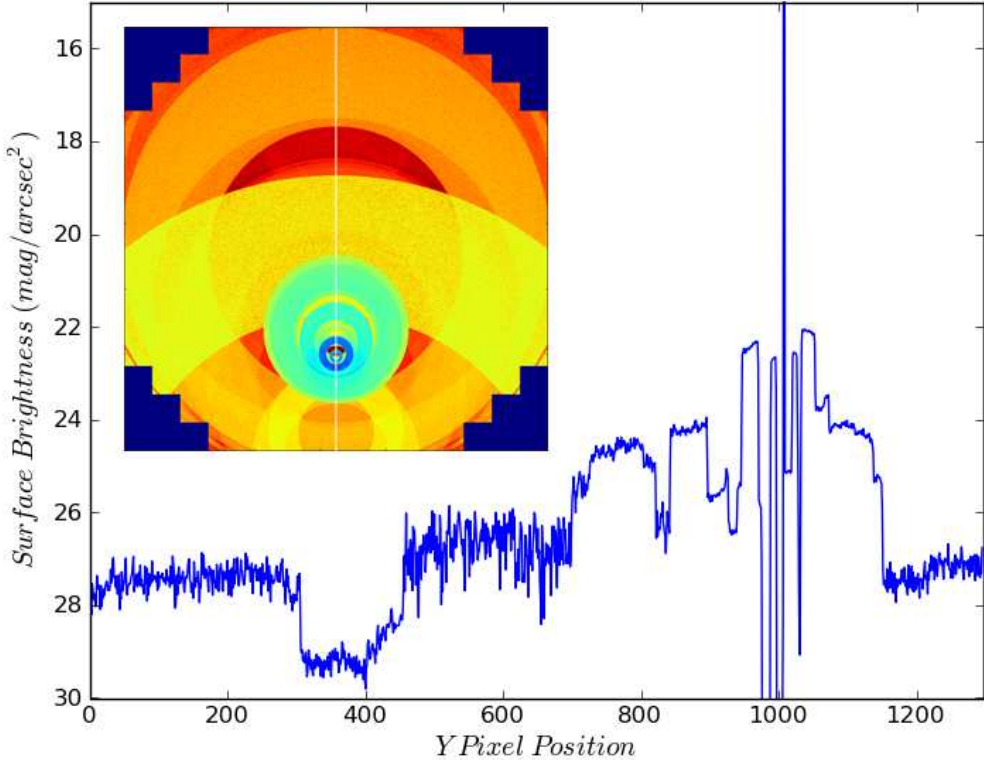


Fig. 4.—: **A simulation of the ghost images resulting from a single, flat SED, zeroth magnitude star in the LSST system.** This simulation was created using a ZEMAX model of the LSST optical system and baseline filters (including all optical coatings and the full ‘recipe’ for the filter layers). The image shows spatial distribution of the ghost images that result, color-coded by surface brightness. The line plot shows the surface brightness of the ghosts along the y axis (at the location of the white line in the image). The brightest ghosts from this single star cluster around the location of the star itself, and are shown in blue. The ‘pupil ghost’ is visible as the large ring nearly tangent to the edge of the field of view, and would contain ghost light from *any* source in the field of view, thus can potentially be the brightest ghost in an image with a large number of sources or high background counts.

To account for these effects (and any remaining ghost or pixel scale variations), a dense network of stars of a variety of spectral types will be rastered across the focal plane on a photometric night. The images will be divided by the observed flat field corrected by a preliminary illumination correction containing corrections for the ghost images and the pixel scale variation. Then the counts for each star will be corrected for varying color terms in the atmosphere and hardware response, as further described in subsection 4.2. The updated illumination correction can then be determined by minimizing over all stars i in all observations j (as in Equation 15, but in slightly different circumstances),

$$\chi^2 = \sum_{i=N_{stars}, j=N_{obs}} \left(\frac{m_{ij}^{meas}(x, y) - m_{ij}^{model}(x, y)}{\sigma_b} \right)^2 \quad (19)$$

where the model magnitude of each star in each observation is given by

$$m_{ij}^{model}(x, y) = m_b, i^{best} - \delta k_{b,j}^{atm+sys}(x, y, alt, az, SED, t) - \int d\lambda dZ_{IC}(x, y, \lambda) \quad (20)$$

where $m_{b,i}^{best}$ is the best-fit, constant magnitude of the star in this filter, $k_{b,j}^{atm+sys}$ is the color-term correction (partially determined by the constant from exposure-to-exposure hardware throughput curve and partially determined by the varying with each exposure atmospheric throughput curve), and dZ_{IC} is the update to the illumination correction which is produced by this dense raster scan. Similar applications of raster scans have been successfully used in previous surveys, (*e.g* Regnault et al. (2009); Magnier & Cuillandre (2004); Manfroid (1996)), providing an illumination correction accurate to the sub-percent level. With the additional information from the modeling of the ghost images, pixel scale variation, and particularly the better intrinsic uniformity of the dome screen illumination, we expect the illumination correction for LSST to be at least factor of 2 more accurate.

The Total Illumination Correction

Illustrative examples of the effects described in detail above for a theoretical dome flat and the corresponding illumination correction are shown in Figure 5, and the effect of this illumination correct on final measured counts are shown in Figure 6.

Illumination corrections (one per filter) will be generated whenever the camera is removed from the telescope or the focal path undergoes significant changes (such as a filter being replaced or the mirrors being realuminized), but should be stable otherwise. The illumination corrections will be created with a combination of forward modeling (generating the ZEMAX model to detail the ghost light contribution and correcting for the pixel scale variation) and dense raster scans of stars (to measure the pixel scale variation and correct for any non-uniformities in the dome screen illumination or stray light).

Further refinements to the illumination correction can be determined by incorporating additional terms into the self-calibration model magnitudes (see Section 4.3).

4.1.2. Error in the Normalization of the Hardware Transmission

The dome screen projectors will be designed to be uniform to better than 1% (10 mmag) across the LSST field of view. After applying the ZEMAX model to generate expected ghost reflections and scattering within the camera, and adding dense raster scans of stars to generate a preliminary illumination correction, this variation will be reduced to approximately 5 mmag (based on the SNLS experience (Regnault et al. 2009)). With the addition of further improvements from the self-calibration procedure, we expect the error due to the hardware normalization to be < 3 mmag.

4.2. Correcting for the Shape of the Hardware and Atmospheric Response Curve

Compensation for the changes in observed magnitudes caused by variations in the wavelength dependence (shape) of the hardware and atmospheric response curves, $\phi_b^{sys}(\lambda)$ and $\phi^{atm}(\lambda)$, will be done using independent measurements of the hardware response curve (generated from the narrow-band flat fields) and the atmospheric response curve (generated from atmospheric extinction models generated from measurements from the auxiliary telescope). While the measurement of the shapes of the hardware and atmosphere curves are independent, the actual correction that must be applied depends on the combination of atmospheric and hardware response curves as well as the SED of the astronomical object. This correction is necessary for precision photometry, but as it requires knowledge of the object’s SED, most LSST reported magnitudes will include either no correction or a (potentially rough) correction along with an indication of what SED was assumed to generate this value. However, for stars which will be used in self-calibration (see subsection 4.3) to determine photometric zeropoints in each exposure, a model SED well-matched to the object’s colors will be chosen and used to generate the Δm_b^{meas} corrections described in this section.

It is worth emphasizing as we start this section that Δm_b^{meas} is a correction for changes in the *shape* of the bandpass only; any grayscale components to the changes in bandpass shape discussed here are not part of Δm_b^{meas} and instead belong to either the hardware or atmospheric *normalization* corrections.

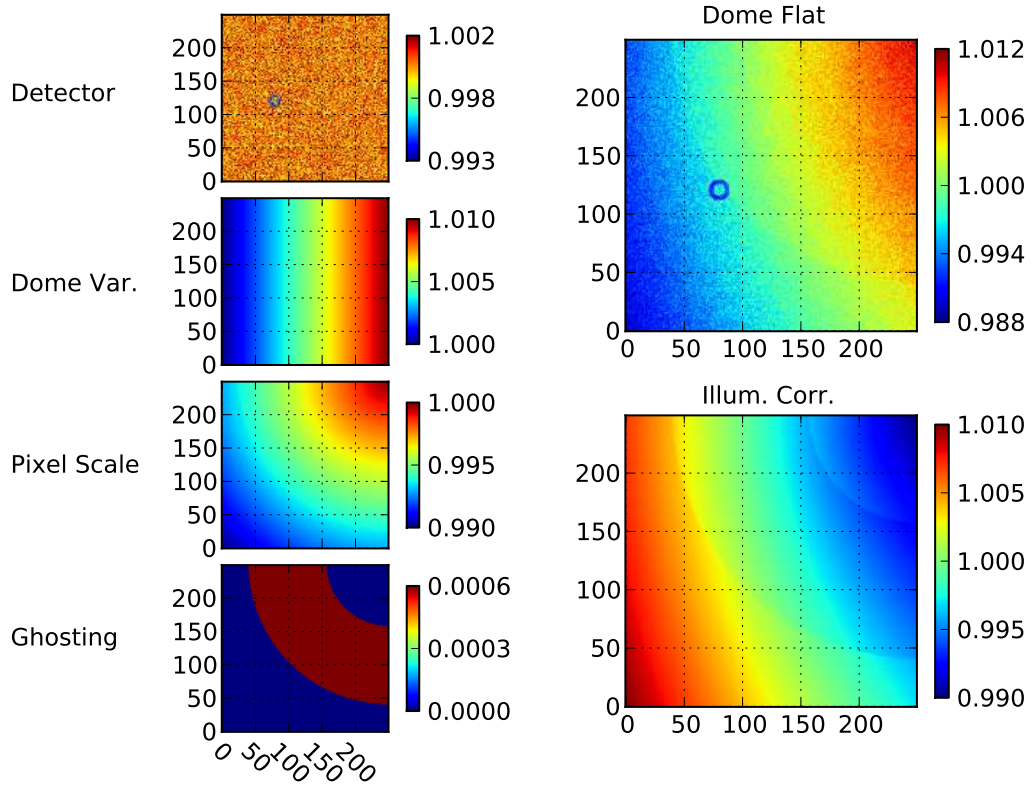


Fig. 5.—: **Components of the illumination correction.** Any flat field obtained from the dome screen includes not only a measurement of small-scale variations in detector sensitivity (Detector panel, top left, including a dust ring (blue ring)), but also records unwanted effects such as variations in the dome screen illumination as a function of position (Dome Var. panel), variations in brightness that result from variations in the amount of sky observed by each pixel (arising from variations in the pixel scale over the focal plane) (Pixel Scale panel), and ghosting caused by internal reflections in the camera (Ghosting panel). Each panel on the left demonstrates the effect on the total flat field attributable to each of these variations, in a simplified manner. Variations are generated as follows: pixel-to-pixel variation in detector sensitivity is 0.4% (as well as a small dust ring), the dome screen has a 1% gradient across the field of view, the pixel scale changes by 0.5% from corner to corner, and the ghosting is generated by adding 0.1% of the total light into a ring reflection. The top large panel on the right shows the dome screen flat field that would be observed after combining all of the effects on the left. The bottom large panel on the right shows the illumination correction that must be multiplied with this flat field to remove the effects of the dome screen variation, the pixel scale variation, and the ghosting. Note that no photon noise was introduced in this simulation.

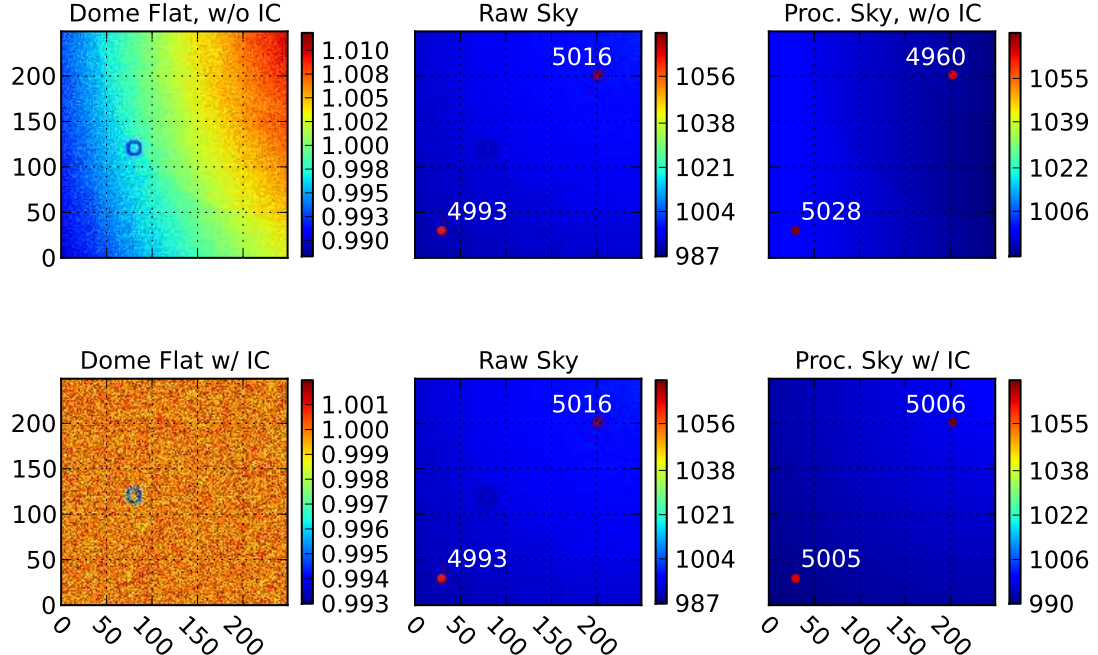


Fig. 6.—: **Effect of illumination correction on photometry.** The left top panel shows a flat field obtained from a dome screen, created with the same conditions (including the same dust ring) as in Figure 5, without multiplying by an illumination correction. The central top panel shows a raw ‘image’ of the sky, generated by adding a background sky value of 1500 counts per pixel (scaled by the pixel area, as in Fig. 5), to two stars. The stars were generated by placing 5000 counts over a circular aperture the size of the PSF at the location of the star. A ghost image was created as in Fig. 5. The right top panel demonstrates the result of processing the raw sky image by subtracting the ghost image and then dividing by the dome flat without an illumination correction. The left bottom panel shows the illumination correction applied to the same flat field. The middle bottom panel shows the same raw sky image as the top row. The bottom right panel demonstrates an improved processing of the raw sky image, by subtracting the ghost image and then dividing by the illumination corrected flat field. Note that the sky background does not appear flat but is correct for preserving stellar photometric accuracy. In every image with stars, the numbers next to each star indicate the counts measured within an appropriate circular aperture for the star. In the raw images, these counts are not equal because of the variation in pixel to pixel sensitivities.

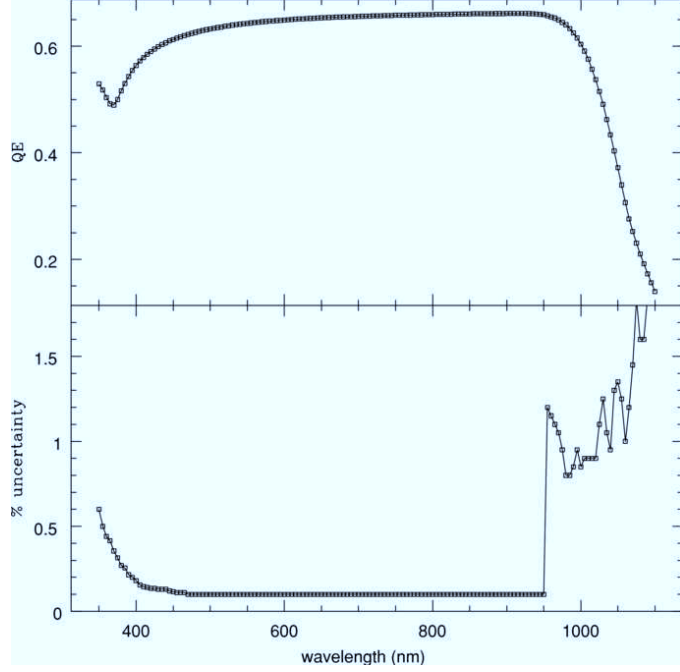
4.2.1. Measuring the shape of the hardware response curve

The dome screen projector system introduced in section 4.1 will be used to generate a series of narrow-band flat fields at wavelengths covering the range of LSST’s sensitivity (approximately 350-1100 nm) in each filter. The same dome screen uniformity requirements for the broadband flat field apply to the narrow-band dome screen illumination; < 1% across the camera field of view (corresponding to < 10% variability across the projector surface) and < 0.25% variability in the focal plane on scales smaller than 0.5°.

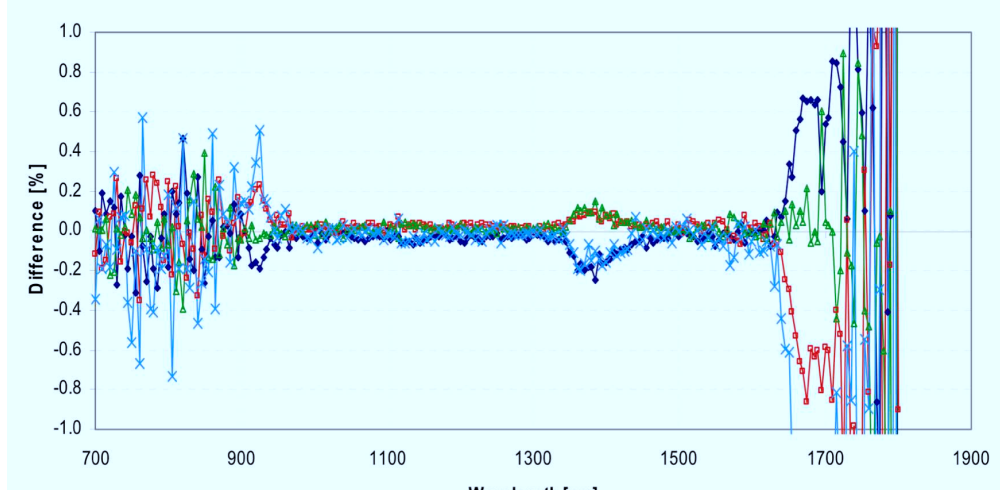
The narrow-band light sources can be adjusted at intervals as fine as 1 nm. A set of precision diodes will be used to normalize the photon flux integrated during flat field exposures, thus allowing a precise comparison of the system response at different wavelengths when using the narrow-band light sources. These photodiodes, together with their read-out electronics, can be calibrated at the U.S. National Institute of Standards (NIST) to $\approx 0.1\%$ relative accuracy across wavelengths from 400 nm to 900 nm (g , r , i , z bandpasses) using current technology. This can be extended to 1600 nm (into and beyond the y band) using techniques under development, which also have the possibility of achieving 0.01% accuracy in the diode calibration at NIST (Eppeldauer et al. 2009), as shown in Figure 7.

Further details of the LSST narrow-band flat field apparatus can be found in Gressler et al. (2010). Preliminary results from a similar apparatus tested at Pan-STARRS can be found in Stubbs et al. (2010), as well as earlier experiments from CTIO described in Stubbs et al. (2007b).

In each filter, a series of narrow-band flats will be taken at a range of wavelengths to form a data cube of flat fields in (x, y, λ) . To measure the total hardware response, each of the narrow-band flats in this datacube must be adjusted by an illumination correction, primarily for ghosting effects (which can be strongly wavelength dependent). The hardware response curve can then be measured at all (or a subset of) x, y positions while the photodiodes track the relative intensity of light produced by the dome screen as a function of wavelength. The narrow-band flats are time-consuming to acquire; scanning through all 6 filters at 1 nm intervals requires many hours worth of exposures and must be done in minimal levels of ambient light. However, any wavelength dependent variations in the synthetic flat are expected to change relatively slowly so the full set of narrow-band flats only need to be acquired approximately once a month, which could be done during cloudy nights.



(a) Stubbs et al. (2010)



(b) Eppeldauer et al. (2009)

Fig. 7.—: Quantum efficiency curve and fractional uncertainty for NIST-calibrated photodiode, from Stubbs et al. (2010) and Eppeldauer et al. (2009). Panel (a): Between 400 and 900 nm, calibration methods already in use in test systems indicate photodiode accuracy is better than 0.1%, as in the bottom part of this panel. The sudden decrease in calibration accuracy below 900 nm is due to calibration methods used by NIST in 2005. Panel (b): More recent photodiode calibration efforts by Eppeldauer et al. (2009) show better than 0.1% accuracy can be achieved to beyond 1200 nm, the limit of detector response for LSST, as shown here in the response curves resulting from multiple scans of a single source using the same photodiode.

The narrow-band flat field illumination correction

The illumination correction for the narrow-band flat fields suffers from similar problems as the broadband flat field illumination correction described in section 4.1.1 but will consist primarily of corrections for ghosting; the other effects are less important. This is because we are interested in measuring the shape of the hardware transmission curve at a variety of x, y locations; we are only interested in the sensitivity at each wavelength relative to the sensitivity at other wavelengths at that particular x, y location. Thus, the ‘illumination correction’ necessary for the narrow-band flat fields is slightly different than the illumination correction necessary for the broadband flat used for hardware normalization; only wavelength-dependent quantities need to be considered. Non-uniformities in the dome screen illumination, as long as they are constant in time and with wavelength, will not be a first-order effect in our result (unlike in the broadband flat field, where the overall normalization of the hardware across all x, y is important). Stray and scattered light, as long as it is relatively wavelength independent, will not be important for the same reason. Pixel scale variations, being constant over all wavelengths, are also not important. However, the ghosting can be strongly wavelength dependent; in particular, at wavelengths near the edges of the bandpass, the ghosting resulting from reflections off the surfaces of the filter itself becomes a significant factor (since the chances of transmission or reflection hover at 50%, increasing the chances of eventually scattering light into the focal plane). As much as 15% of the light in the exposure can originate from ghosts near the edges of the bandpass (Stubbs et al. 2010) (see section 4.1.1). Because we are looking for relative sensitivities as a function of wavelength at particular x, y locations, an increase in the total photons captured by the detector due to an increase in ghosting (rather than direct light from the dome screen projector) will be the most significant contributor to the illumination correction.

The same ZEMAX model that is used to generate corrections to the broadband flat field will be used to generate corrections for the ghosts in the narrow-band flat fields (which assumes that the dome screen illumination is uniform; we know the SED of the narrow-band light emitted by the dome screen itself). This will provide the overwhelming majority of the correction necessary for the narrow-band flats. Further checks on this correction can be achieved by measuring the wavelength-dependent sensitivity of individual components of the LSST system; Regnault et al. (2009) found that the color-dependent terms they determined from the CFHT photometric grid stars were well reproduced by synthetic photometry and laboratory scans of the filter response as a function of radius.

As with the overall normalization of the hardware throughput (the broadband flat fields), further refinements to the hardware throughput curves can be determined by incorporating additional terms into the self-calibration model magnitudes (see section 4.3). However it is

important to note that these additional refinements will only be completely correct for main sequence stars (the calibration stars themselves), as the main sequence stars (and thus their SEDs) are the only objects incorporated into the self-calibration procedure.

The expected effect of $\phi_b^{sys}(\lambda)$ variations

It is expected that the shape of the response curve will be primarily a function of radius due to variations in the thickness of the filter coatings caused by the mechanism used to deposit those coatings. The variation due to filter nonuniformities is specified to be less than 1% across the focal plane, most likely in the form of a bandpass shift as shown in Figure 8. For main sequence stars, the resulting changes in observed magnitude as the bandpass shifts by 1% of the central wavelength can be as much as than 0.04 magnitudes (40 mmag) - and even larger in the u band (see Figure 9). However, as long as the variation in the hardware response curve at each x, y location is measured to better than 0.05%, the maximum error contribution towards calibrating these observed magnitudes will be less than 2 mmag for all bandpasses other than u , where the error could be as much as 5 mmag for certain main sequence stars (see Figure 10). This is equivalent to approximately a 3 Angstrom error in wavelength calibration of the monochromatic light source throughout the bandpass or a 0.5% error in photodiode calibration assuming that the shape of each bandpass is determined using at least 100 independent measurements (i.e. 1 measurement every few nanometers within the bandpass).

Because the shape of the hardware response curve varies as a function of filter radius, it is also necessary to monitor any offsets of the filter position from dead center after any filter changes. Assuming the filter response curve varies linearly with radius, the filter location must be measured to better than 0.025% (half of the 0.5% error in hardware curve measurement above) for the filter positioning to remain less than a 1 mmag source of error. Given the filters are approximately 75 cm in diameter, this means the filter positioning must be recorded to better than 0.2 mm.

4.2.2. Measuring the shape of the atmospheric transmission curve

The shape of the atmospheric transmission curve appropriate for each observation will be generated using data from spectroscopic measurements of bright stars obtained with the LSST auxiliary telescope. These measurements will be fit to a model of atmospheric absorption extinction (which includes how this absorption varies across the sky and over time as well as atmospheric extinction profiles generated by MODTRAN (Berk et al. 1999;

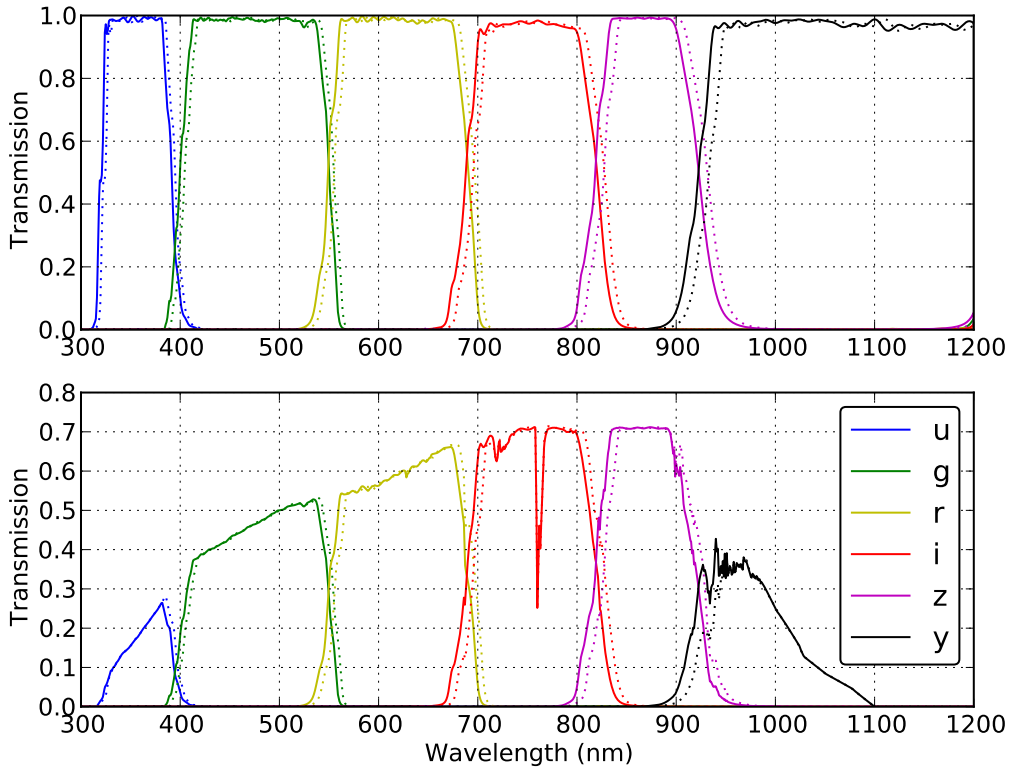


Fig. 8.—: **Baseline filter curves and a potential (1% of the central wavelength) shift due to nonuniformity in the filter bandpass.** The solid lines indicate standard filter bandpasses (top panel: filter alone, bottom panel: filter plus standard mirror, lens, detector and atmosphere response curves) while the dashed lines indicate the same bandpass shifted redward by 1% of the central wavelength.

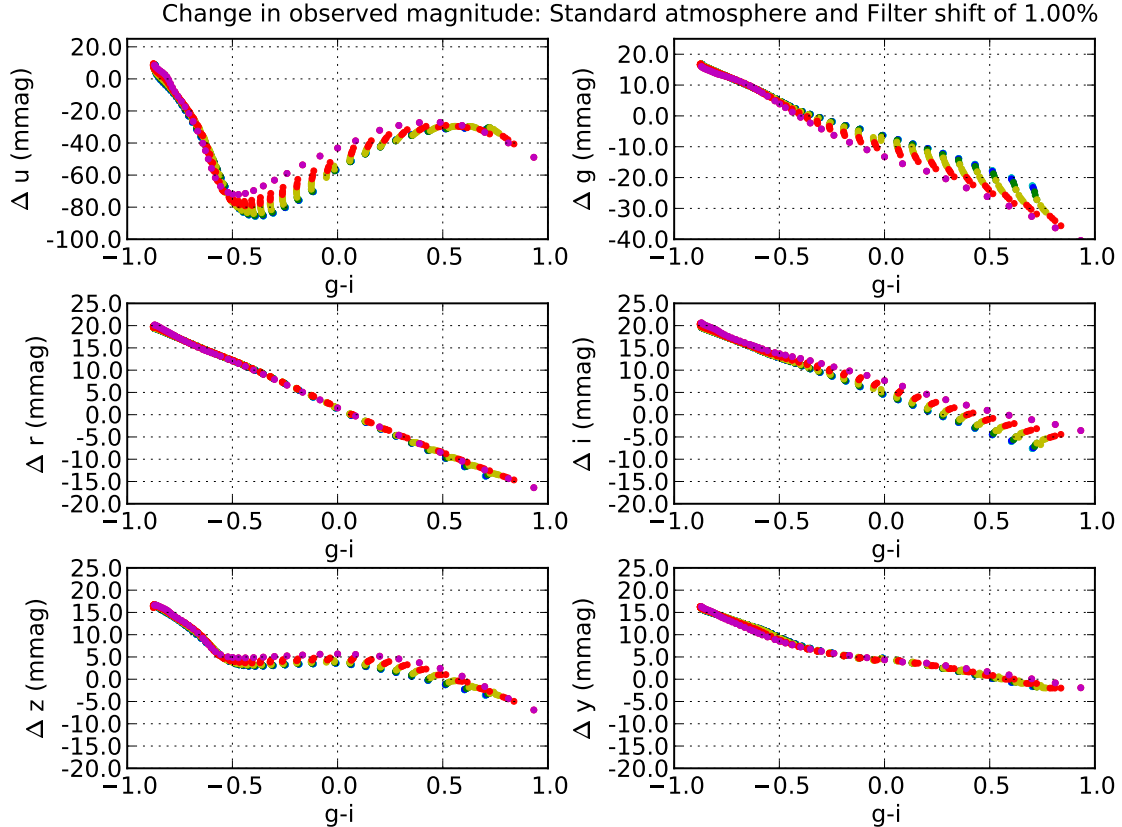


Fig. 9.—: Δm_b^{obs} due to a hardware response curve shift of 1% of the central wavelength of each bandpass. 850 main sequence star Kurucz models with temperatures between 5000K and 35000K and metallicity indexes between -5.0 and 1.0 (solar) were combined with a standard atmosphere and standard hardware bandpass, and then with a total system response where the atmosphere remained constant but the hardware response was shifted by 1% of the central wavelength of each bandpass (as in Fig 8). The points in each plot are color-coded by metallicity, in steps of 1 dex between -5.0 (blue) to 1.0 (magenta). The resulting changes in observed natural magnitudes are on the order of 20 mmag typically, except in u band where the shift can create a δu of closer to 80 mmag for certain temperatures of main sequence stars. By measuring the bandpass shape as a function of radius and the colors of the main sequence stars, we can remove these effects.

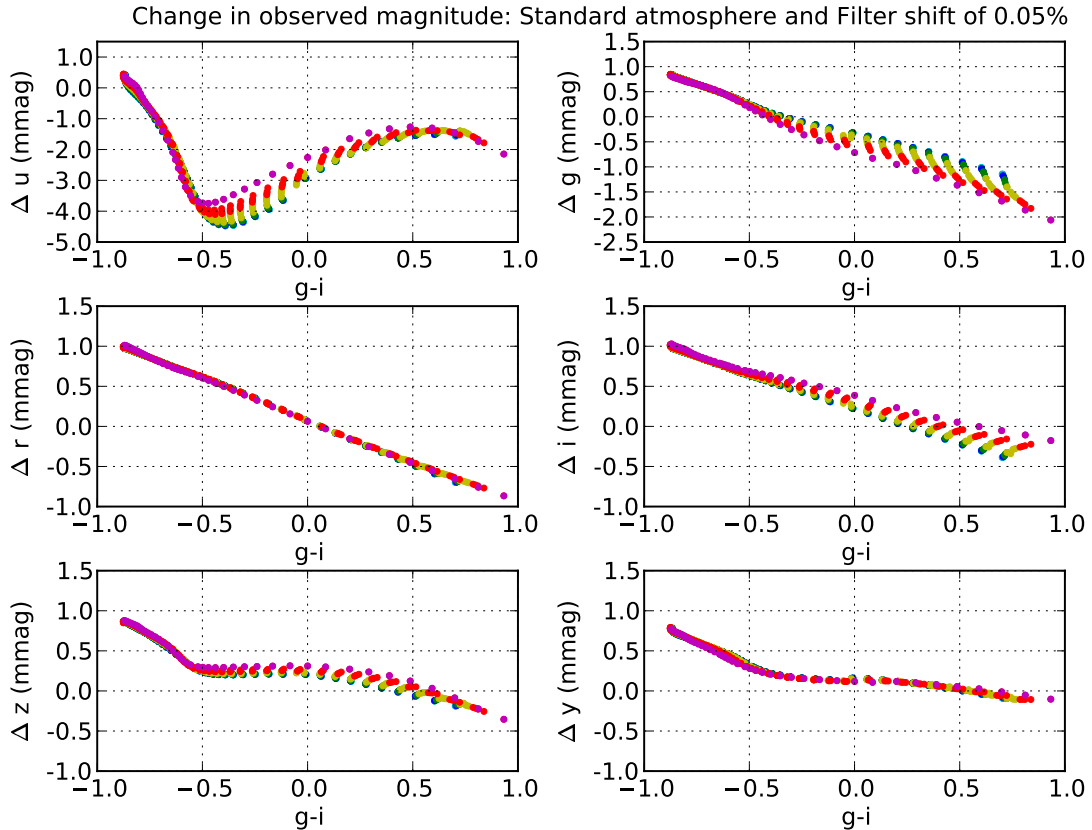


Fig. 10.—: Δm_b^{obs} due to a hardware response curve shift of 0.05% of the central wavelength of each bandpass. Similar to Fig 9 except that the hardware response was shifted by only 0.05% of the central wavelength, an amount representing an unmeasured shift in the hardware response and thus contributing directly to the final error in the calibration of the natural magnitudes. Note that the y scale in these plots is reduced by a factor of 20 from Figure 9, consistent with measuring and compensating for the bandpass shift to within a 0.05% error.

Anderson et al. 2001)) to determine the atmospheric transmission profile at all points on the sky at all times.

Atmospheric absorption behavior

The shape of the atmospheric transmission curve, $\phi^{atm}(\lambda, alt, az, t)$, is determined by three major sources of atmospheric extinction: molecular scattering (Rayleigh scattering), aerosol scattering (Mie scattering), and molecular absorption.

- Molecular scattering, or Rayleigh scattering, is due to elastic scattering off atoms and molecules in the air. Atmospheric absorption due to Rayleigh scattering has an optical depth

$$\tau \propto (\lambda/\lambda_o)^{-4} (BP/BP_o), \quad (21)$$

where BP is the barometric pressure (Hansen & Travis 1974), and BP_o is a reference value (typically around 782 mb for Cerro Tololo). The total atmospheric extinction due to Rayleigh scattering is thus driven only by pressure variations and is proportional to airmass,

$$S(\lambda, X) \propto e^{-\tau, X}, \quad (22)$$

and is also axisymmetric around the zenith. Changes in the optical depth due to Rayleigh scattering typically will produce < 1 mmag change in the observed counts.

- Aerosol scattering, or Mie scattering, occurs when visible light is scattered by particles suspended in the atmosphere with a size similar to its wavelength. This gives rise to an absorption curve with a strongly variable total column depth as well as a variable wavelength dependence, where

$$\tau \propto (\lambda/675\text{nm})^\alpha. \quad (23)$$

The index α has been measured to range between -0.9 to -1.7 in observations from CTIO (Burke et al. 2010). Stubbs et al. (2007a) measured the aerosol optical depth at Mauna Loa, recording total aerosol optical depths at zenith varying from ≈ 0 to 0.3 (generally < 0.1) at $\lambda = 440$ nm, with maximum rate of change $\approx 0.02/\text{hr}$. The atmospheric extinction τ due to aerosol scattering scales directly with airmass, but is not necessarily axisymmetric around zenith, often showing a trend in the East-West direction.

- Molecular absorption produces a more complex set of absorption bands and features, originating from line absorption due to ozone (O_3), water (H_2O), oxygen (O_2) and

other trace species (OH, N₂O, etc.). The resulting atmospheric absorption features are largely due to narrow saturated Lorentzian-shaped lines spaced closely in wavelength and, due to this saturation, scale non-linearly with airmass,

$$S(\lambda, X) \propto e^{-\tau \sqrt{X}} \quad (24)$$

as in Stubbs et al. (2007a). The total column depth for O₂ and other trace species is related directly to the square root of the column depth for molecular scattering, and is thus proportional only to the square root of the barometric pressure and airmass. However, O₃ and H₂O absorption is more variable. O₃ absorption can vary by 5–10% day to day, with seasonal variations of 25% or so, but is expected to be non-variable across the sky and closely correlated with satellite data on total ozone content. H₂O absorption can vary on timescales as short as 10–20 minutes, and is expected to show linear trends across the sky (East-West and North-South).

Figure 11 demonstrates the wavelength dependency of each of these components and how they change with airmass.

Fitting the atmospheric absorption

Using MODTRAN we can generate atmospheric transmission profiles at a variety of airmasses for each of these major sources of atmospheric extinction – molecular (Rayleigh) scattering, aerosol (Mie) scattering, and molecular absorption from each of O₃, H₂O, and combined O₂/trace species, as is shown in Figure 11 for a standard atmospheric composition (the 1976 US Standard). These profiles capture the wavelength dependence of each component individually, over a grid of airmasses, and can be used as templates to generate new atmospheric transmission curves for any desired atmospheric composition as follows:

$$\begin{aligned} S^{fit}(alt, az, t, \lambda) = & e^{-\tau_{aerosol}(alt, az, t, \lambda) X} \\ & \times (1 - C_{mol}(BP(t)/BP_o) A_{Rayleigh}(X, \lambda)) \\ & \times (1 - \sqrt{C_{mol}(BP(t)/BP_o)} A_{O_2}(X, \lambda)) \\ & \times (1 - C_{O_3}(t) A_{O_3}(X, \lambda)) \\ & \times (1 - C_{H_2O}(alt, az, t) A_{H_2O}(X, \lambda)). \end{aligned} \quad (25)$$

The $A_{Rayleigh/O_2/O_3/H_2O}$ functions are absorption templates (i.e. 1 minus the transmission profiles from the MODTRAN models), the C_{mol,O_3,H_2O} are coefficients describing the composition of the atmosphere together with $\tau_{aerosol}$, and $BP(t)$ is measured. An example of an atmosphere generated in this fashion is shown in Figure 12, demonstrating that this method

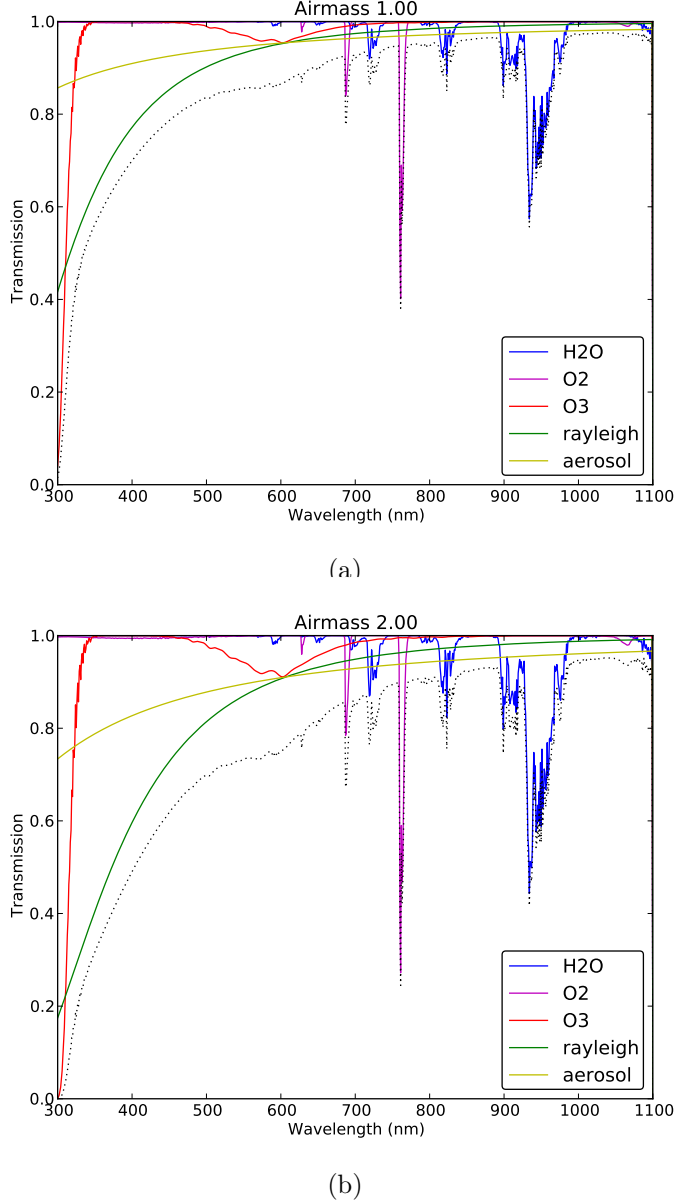


Fig. 11.—: **Components of atmospheric absorption.** The wavelength dependence of the various components of atmospheric absorption at zenith (panel a) and at airmass=2.0 (panel b) is shown here. The H₂O (blue) and O₃ (red) molecular absorption contributions are shown separately, while the O₂ absorption is combined with other trace elements (magenta). A typical example of aerosol scattering (Mie scattering) is included (yellow), as is molecular scattering (Rayleigh scattering) (green). All components except aerosol scattering were generated using MODTRAN4 with the US Standard option (aerosol scattering is not part of the US Standard atmosphere). The resulting total absorption curve is the product of each of these effects and is shown with the dotted black line. This is an illustrative atmosphere; under actual observing conditions the molecular absorption components will vary in strength with time and the square root of the airmass, the molecular and aerosol scattering will depend on airmass, and the aerosol scattering profile will also vary with time.

can be used to generate an atmosphere at any airmass for any composition desired, without needing to generate a full MODTRAN model.

With this capability, we can fit the auxiliary telescope spectroscopic data taken throughout the night for the values of C_{mol,O_3,H_2O} , increasing our SNR for these coefficients by modeling their expected behavior over time and across the sky as detailed in 4.2.2 above. The Rayleigh scattering and molecular absorption due to O₂ and other trace species are fit with a single coefficient, C_{mol} , which simply scales the MODTRAN templates to the appropriate level for Cerro Pachon, and then only change with the barometric pressure (*BP*). The O₃ absorption is fit with a single C_{O_3} value for each night, as it is not expected to vary more than 5-10% within a night. The aerosol absorption, as it is expected to have a small spatial variation across the sky, is modeled as

$$\tau_{aerosol}(alt, az, t, \lambda) = (\tau_0 + \tau_1 \text{EW} + \tau_2 \text{NS}) \left(\frac{\lambda}{\lambda_0} \right)^\alpha, \quad (26)$$

where EW and NS are defined as EW = cos(*alt*)sin(*az*), NS = cos(*alt*)cos(*az*), projections of the telescope pointing in the EW/NS directions. Single values of τ_0 , τ_1 , τ_2 and α are fit for each night of observing, with τ_1 and τ_2 likely to be very small (Burke et al. 2010). The H₂O absorption is likewise expected to show spatial variation, but also time variability, and is modeled as

$$C_{H_2O}(alt, az, t) = C_{H_2O}(t) + \frac{dC_{H_2O}}{d\text{EW}} \text{EW} + \frac{dC_{H_2O}}{d\text{NS}} \text{NS} \quad (27)$$

using a constant spatial EW and NS gradient per night and a $C_{H_2O}(t)$ that is fit to each auxiliary telescope measurement (and interpolated between these times).

The coefficients $C_{mol/O_3/H_2O}$ and $\tau^{aerosol}$ will be determined using spectra of bright stars obtained from the 1.2-m LSST auxiliary telescope. The auxiliary telescope will be equipped with a modest resolution ($R \sim 400$) spectrograph, sufficient to capture the signatures of the atmospheric extinction components, and covering the entire wavelength range of LSST ($300 < \lambda < 1100$ nm) in each exposure. The stars observed with the auxiliary telescope must be bright ($r < 12$) and ideally either white dwarfs or F stars – stars with relatively simple and well-understood SEDs to minimize confusion with the atmospheric extinction. By observing the same grid of stars on multiple nights, even if the SEDs are not well determined initially, they can be bootstrapped from the many epochs of data.

Generally, the auxiliary telescope will *not* observe stars along the same line of sight as LSST, as the values for $C_{mol/O_3/H_2O}$ and $\tau^{aerosol}$ are better constrained by observing a wide variety of airmasses and locations on the sky that cover a wide range in N/S/E/W directions, as well as utilizing repeat observations of the same star throughout each night, and then fitting the spectroscopic data from the entire night. This improves the signal to noise for the atmospheric absorption profiles generated for each science observation.

The expected effect of $\phi_b^{atm}(\lambda)$ variations

Burke et al. (2010) describes a series of observing runs at CTIO carried out over several months, where spectroscopic observations of stars were fit using this method. Using the extremes of the range of C_{mol} , C_{O_3} , C_{H_2O} , τ_i and α parameters from these runs, Figure 13 shows the resulting changes in observed magnitudes due to the changes in bandpass shape when applied to our set of main sequence star Kurucz models. Varying C_{H_2O} only affects the z and y bands, while changing C_{O_3} , τ_0 , and α affect the u and g and, to a lesser extent, r bands. Using these ‘worst-case’ parameters, at $X = 1.2$ we find differences in the observed natural magnitudes on the order of $\Delta u = 14$ mmag, $\Delta g = 7$ mmag, $\Delta r = 4.5$ mmag, $\Delta i = 1.5$ mmag, $\Delta z = 2$ mmag, and $\Delta y = 7$ mmag. The atmosphere transmission curves used to generate this data, and a plot of the resulting Δm_b^{obs} are in Figures 14 and 15. These represent the induced changes in observed counts due to changes in the bandpass shape; however, by achieving 10% accuracy on $\tau^{aerosol}$, C_{O_3} , and C_{mol} , and 30% accuracy for C_{H_2O} , we can correct for these effects to within 1 mmag in all bands except y , where it remains 2 mmag. The limits on remaining uncorrected effects are shown in Figure 16.

Changes in airmass have a larger effect on observed natural magnitudes (Figure 17) than the variation in atmospheric extinction coefficients. However, these are included in the atmospheric extinction templates generated by MODTRAN and can be accurately corrected. Within the LSST 3.5° diameter field of view, the difference in airmass from top to bottom of the field can be considerable, and must be included in the model.

4.2.3. Errors in the shape of the hardware and atmospheric response

Correcting observed counts for the difference between the measured shape of the hardware and atmospheric response curves and the standard normalized bandpass, $\phi_b^{std}(\lambda)$, requires knowledge of the SED of each star. However, with this knowledge (which comes from the colors of each star), it is possible to create lookup tables of $\Delta m_b^{meas}(x, y, alt, az, SED, t)$ (as in Equation 17) for various locations in the focal plane in each exposure. A rough example is given in Table 1.

Assuming that the errors in the combined shape of the hardware and atmospheric response curves add in quadrature, with the limits described above (2 mmag error in *grizy*, 5 mmag error in *u* due to the hardware response curve; 1 mmag in *ugriz*, 2 mmag error in *y* due to the atmospheric response curve), the final error in observed magnitude due to both of these effects would be < 3 mmag in *grizy* and 5 mmag in *u*. There is an additional potential source of error in these Δm_b^{meas} corrections – understanding of the true SED of the

source. However, Δm_b^{meas} varies only slowly with changes in $g - i$ color and metallicity for these main sequence stars, so if the color is known better than 0.02 mags and the metallicity is determined to better than 2 dex, the error introduced by applying an incorrect Δm_b^{meas} is less than 1mmag.

4.3. Normalization of the Atmospheric Transmission

After applying each of the previous corrections, the raw counts have been corrected to a ‘standard’ bandpass for each filter, $\phi_b^{std}(\lambda)$, using both the narrow-band flats and the atmospheric model derived from the auxiliary telescope observations. Gray-scale zeropoint variations (particularly on small scales, < several times the PSF) across the focal plane due to the telescope hardware system have also been removed by the synthetic flat. However, there still remain variations in the normalization of the system response that result from gray extinction due to clouds. The primary driver for the self-calibration procedure is to correct for these gray zeropoint offsets that result from atmospheric variations; a secondary use for the self-calibration is to reduce any other systematic errors.

The self-calibration procedure selects bright, isolated main sequence and white dwarf stars (or any star with well-known colors and a well-known SED, to reduce errors in the applied δk values) from the sample of all observed stars after they are corrected to the standard bandpass (‘standardized’). Only non-variable stars will be selected for self-calibration, based on approximately calibrated data (say, a few percent) which will suffice in this context. It then uses the many repeat observations j of each star i in a particular filter to minimize Equation 15,

$$\chi^2 = \sum_{ij} \left(\frac{m_{b,ij}^{std} - m_{b,ij}^{model}}{\sigma_{b,ij}^{std}} \right)^2, \quad (28)$$

where the m_{model} includes any remaining photometric corrections that must be applied. In the most basic calibration plan, the model magnitude would only include a single gray extinction zeropoint offset per patch due to clouds, applied as in Equation 16,

$$m_{b,ij}^{model} = m_{b,i}^{best} - \delta z_{b,j}, \quad (29)$$

where the size of each patch is approximately one CCD and $\delta z_{b,j}$ is constant over the patch. A more complicated model magnitude could be used if found desireable. This could include a $\delta z_{b,j}(x, y)$ using higher order functional form in x, y than a simple constant. Simulations of the Milky Way created using the GALFAST model from Mario Juric (available at <http://mwscience.net/trac/wiki/galfast>, based on measurements of stellar distributions from SDSS) indicate that there will be approximately 50–100 suitable calibration stars per patch

over the entire sky – easily enough to support a higher order zeropoint determination. This model magnitude could also include additional corrections for the hardware normalization (essentially, terms to refine the illumination correction defined in Section 4.1.1), or terms which depend on the color of the stars (essentially, terms to refine the hardware bandpass calibration), assuming those terms were constant for long stretches (approximately a year’s worth) of time.

Minimizing Equation 15 requires solving for approximately, $10^8 m_{b,i}^{best}$ and $10^8 \delta z_j$, in the basic calibration model. Adding additional terms to refine the calibration of the hardware normalization or bandpass shape increases the number of parameters that must be fit for only slightly, as these terms are assumed constant over large stretches (years’s worth) of observations. Of course, not all stars will be observed on all calibration patches, so there will be only about 10^{10} non-zero values of $(m_b^{std})_{ij}$ (per band). Investigations using a conjugate gradient method to compute m_b^{best} and δz_j for approximately 10^6 stars and 10^6 patches were very successful; the same method could be relatively easily parallelized for the full data set. We have also had preliminary success with simulations using a least squares method to invert the matrix from Equation 15 and solve for $m_{b,i}^{best}$ and δz_j .

With the known values of $(\delta z)_j$, all measurements for all stars from a patch can be re-calibrated, then analyzed for systematics in $[(m_b^{std})_{ij} - (m_b^{best})_i]$ and $[(m_b^{obs})_{ij} - (m_b^{best})_i]$ residuals (e.g., as a function of observation time, position on the focal plane, airmass, seeing, stellar color, brightness, seeing, etc.). The self-calibration step can be repeated if necessary, with corrections for any discovered systematics incorporated in the next-iteration values for $(m_b^{std})_{ij}$. Alternatively, fits for parameterizations of these systematics can be added directly into the model magnitudes used for the self-calibration solution, as described above.

Investigations of this final step in the internal calibration procedure are detailed in the LSST self-calibration document produced by Yoachim, et al. These investigations use a simulated stellar catalog generated with Mario Juric’s GALFAST code. This stellar catalog covers the entire sky with the exception of the plane of the Milky Way, with more than 10^6 stars over the magnitude range between $16 < r < 21$. Individual ‘observations’ of each star are generated by combining this ‘truth’ stellar catalog with a simulated pointing history from the LSST Operations Simulation team (OpSim v3.61, available at http://opsimcv.s.tuc.noao.edu/data_access/download_data.html). For each observation, the true magnitude is offset by terms which correspond to signal-to-noise considerations appropriate for the observation conditions and cloud extinction (represented by a potentially large zeropoint offset combined with a smaller gradient across each patch). Additional offset terms corresponding to flat field and illumination correction errors and/or color terms related to uncorrected hardware filter curve variations and atmospheric extinction effects have

been included in tests of the self-calibration; further offset terms, such as clumpier cloud extinction, are under investigation as well.

When these offsets correspond to values within the range of the expected uncorrected errors discussed in each section above (sections 4.1, 4.2.1, 4.2.2), the self-calibration procedure is able to fit for $m_{b,i}^{best}$ and δz_j values which meet the SRD requirements (10 mmag uniformity and 5 mmag repeatability for the stars in the simulation). This fit converges to meet the SRD requirements after slightly less than 2 years of observations, or about 24 visits per star; with more observations, photometric uniformity continues to improve.

A set of example plots corresponding to a baseline self-calibration test are shown in Figure 18. In this simulation, observations over two years with Declination between -80 and 0 degrees were used; regions slightly further north or south are part of OpSim, but they because they are not part of the main footprint of the survey often receive fewer visits and thus skew the results of these investigations. Observations for each star were generated with the following offsets: random gray offsets for cloud extinction (between 0-1.0 magnitudes of extinction, uniform across the field of view plus a gradient of up to 5mmag across each patch); a color term corresponding to an uncorrected radial gradient in the filter bandpass (constant over time), along with a random jitter in the filter placement; a color term corresponding to an uncorrected atmospheric extinction effect (varying for each visit); and a constant gray offset corresponding to errors in the photometric flat field (varying slowly across the field of view). Each of these offsets were applied with values consistent with those expected from the sections above.

After running the self-calibration procedure to generate simple δz_j values for each patch, the map of residuals between the calibrated magnitudes ($m_{b,i}^{cal} = m_{b,i}^{meas} - \delta z_j$) and the best-fit magnitudes ($m_{b,i}^{best}$) was examined to search for remaining systematics. These systematics (which would include the radial color term and photometric flat field error) were incorporated into an updated $m_{b,i}^{cal}$ value, and the self-calibration procedure rerun on the new values. This process was iterated once more to produce the plots shown in Figure 18. As can be seen, the distribution of best-fit vs. true magnitudes of the stars has an RMS of 4.1 mmag (well below the SRD requirement on uniformity of 10 mmag), while the RMS of the calibrated vs. true magnitudes has a median value of 5.0 mmag (consistent with the SRD requirement on repeatability of 5 mmag).

This self-calibration procedure can be successful only if patches overlap on the sky, so that the same star is observed on multiple patches. This means complete sky coverage is necessary to link all stars together into a rigid system, but also indicates that some amount of dither is required. These investigations have shown that dither patterns where the overlap is one quarter of the field of view or more produce results meeting the SRD requirements.

Note that $m_{b,i}^{best}$ and δz_j are constrained only up to an arbitrary additive constant. For convenience, this constant can be set so that stars have roughly correct AB magnitudes, however the goal after self-calibration is primarily to have a rigid, self-consistent magnitude system, equivalent to the natural magnitudes. Accurately calibrating the internal magnitudes to an external scale is discussed in the next section, Section 5.

4.3.1. Photometric vs. Non-photometric data

Correcting for the color terms resulting from the difference between $\phi_b^{meas}(\lambda, t)$ and $\phi_b^{std}(\lambda)$ requires some preliminary measurement of the color of each calibration star (to within 0.02 magnitudes). This means we must either have some prior knowledge of the colors of each star (from Gaia, for example) or we must have some other method for measuring colors in the *ugr* bands relevant to determining metallicity and the color corrections detailed in Section 3.1.1, presumably by measuring the magnitudes of these stars in photometric data. Without this requirement, we could just combine all photometric and non-photometric data in the self-calibration routine, leaving the self-calibration solver to determine the appropriate δz_j to compensate for any non-photometric images.

Assuming that we must first identify and use photometric data to determine the colors of each object, this could proceed as follows. Identify all observations which were obtained in relatively photometric conditions by searching for images where the average scatter in magnitude measured for each source was less than some threshold (say < 0.05 magnitudes). Using these images and standard stars in these images, measure a preliminary color for each object. With this preliminary color, make a correction for Δm_b^{meas} and run the self-calibration solver for this (photometric) subset of the data. Iterate the results of the self-calibration solver to improve the color determination for each star, until the color measurement converges to within 0.02 magnitudes.

At this point, we have colors accurate enough to apply a Δm_b^{meas} correction sufficient to run self-calibration on all images, including the non-photometric data.

5. Fixing LSST to an external scale

The next two subsections describe how the internally calibrated natural magnitudes, independently calibrated in each filter bandpass, are fixed to an external scale such that the flux in a single band can be compared to the flux in another filter band (SRD requirement 3) and that the flux in a particular filter band can be compared to an absolute external system

(SRD requirement 4). This is equivalent to determining Δ_{b-r} and Δ_r from Eqn 18.

5.1. Band to band (color)

The band to band calibration for each filter b (the Δ_{b-r} values) will be determined by measuring the flux from one or more celestial objects whose physics are believed to be well understood. In principle, a single object with known colors would be sufficient, however many objects across the LSST footprint will be used to evaluate possible systematic effects in the internal calibration process.

Hot hydrogen (DA) and helium (DB) white dwarf stars have simple atmospheres that are reasonably well understood (model colors are currently reliable to about 0.01 magnitudes). It is estimated that there will be $\approx 100/10$ DA/DB WD stars with $r < 24$ in each LSST image at the South Galactic Pole, although in theory only one of well-measured standard would be required. These WDs will be recognizable from color-color plots (see Ivezić et al. (2007a) Figure 24 for an example). Catalogs of WD stars visible from Cerro Pachon have been constructed (Bergeron 1992; Bohlin & Gilliland 2004), and a ‘white dwarf calibration system’ has been developed (Holberg & Bergeron 2006). The locus of main sequence stars in color-color space is also reasonably well understood and has been used to calibrate photometry with success in previous surveys (MacDonald et al. 2004; Ivezić et al. 2007b). The use of the main sequence stellar locus in addition to WD stars will provide a valuable check on systematic effects that may arise from using (primarily) white dwarfs in the determination of $\phi^{atm}(\lambda, alt, az, t)$, as white dwarfs are bluer than most of the main sequence stars used for the bulk of the remainder of the calibration procedures. Additional checks on the quality of color calibration will be based on color residuals when determining photometric redshifts for galaxies. Analyzing these residuals as a function of galaxy brightness and color, and across the LSST footprint, will yield detailed quantitative estimates of the calibration quality. Although in theory one well-measured standard is all that would be necessary to determine Δ_{b-r} values for each bandpass, in practice having multiple standard with varying colors will serve as a check on systematics and provide estimates of the calibration uniformity throughout the survey.

The values for Δ_{b-r} will be determined by generating model m_b^{std} values for each band-band calibration object, then minimizing

$$\chi^2 = \sum_i \left(\frac{(m_{b,i}^{std} - m_{r,i}^{std})^{meas} - (m_{b,i}^{std} - m_{r,i}^{std})^{model}}{\sigma_{b-r,i}} \right)^2. \quad (30)$$

This comparison can be done using subsets of objects from low Galactic extinction regions,

and then bootstrapping to the entire sky to check for systematic effects.

5.2. Single bandpass to external flux system (absolute scale)

After determining the band to band calibration, there is one further value required to calibrate the entire system to an absolute flux scale: Δ_r . This could again be determined using a single object with a well-known flux and spectral energy distribution, however multiple external calibrators provide a valuable check on systematic effects.

Several WDs in the Northern hemisphere have been very precisely calibrated with HST STIS measurements (Bohlin & Gilliland 2004) and it should be possible to obtain similar HST measurements of one or more targets for use in the Southern hemisphere. Identification of these targets has not yet been completed. Nevertheless, as a result of calibration efforts to support the SDSS-II SNe survey, the absolute calibration of the SDSS Stripe 82 region in the r band is believed to be accurate at the 0.01 mag level (Frieman et al. 2008).

Another route to calibrating to an external flux system is to use standards from Gaia. These will have the advantage of being numerous and widely spread across the sky, with a useful overlapping magnitude range between $r = 16$ to $r = 20$. The magnitude measurements of stars calibrated with the LSST calibration procedure described in this document can be transformed to synthetic magnitudes in Gaia’s bandpasses and compared to Gaia measurements. This comparison across the LSST footprint and as a function of stellar brightness and color will provide a powerful independent test of the quality of LSST photometric calibration.

REFERENCES

- Anderson, G. P. et al. 2001, in Society of Photo-Optical Instrumentation Engineers (SPIE) Conference Series, Vol. 4381, Society of Photo-Optical Instrumentation Engineers (SPIE) Conference Series, ed. S. S. Shen & M. R. Descour, 455–459
- Bergeron, P. 1992, JRASC, 86, 309
- Berk, A. et al. 1999, in Society of Photo-Optical Instrumentation Engineers (SPIE) Conference Series, Vol. 3756, Society of Photo-Optical Instrumentation Engineers (SPIE) Conference Series, ed. A. M. Larar, 348–353
- Bohlin, R. C., & Gilliland, R. L. 2004, AJ, 128, 3053
- Burke, D. L. et al. 2010, ApJ, 720, 811

- Eppeldauer, G. P., Yoon, H. W., Zong, Y., Larason, T. C., Smith, A., & Racz, M. 2009, *Metrologia*, 46, 139
- Frieman, J. A. et al. 2008, *AJ*, 135, 338
- Gressler, W. J., Doherty, P., Krabbendam, V. L., Liang, M., Saha, A., Stubbs, C. W., & Vaz, A. 2010, in Presented at the Society of Photo-Optical Instrumentation Engineers (SPIE) Conference, Vol. 7739, Society of Photo-Optical Instrumentation Engineers (SPIE) Conference Series
- Hansen, J. E., & Travis, L. D. 1974, *Space Sci. Rev.*, 16, 527
- Holberg, J. B., & Bergeron, P. 2006, *AJ*, 132, 1221
- Ivezić, Ž. et al. 2007a, *AJ*, 134, 973
- . 2007b, *AJ*, 134, 973
- Kurucz, R. L. 1993, *VizieR Online Data Catalog*, 6039, 0
- MacDonald, E. C. et al. 2004, *MNRAS*, 352, 1255
- Magnier, E. A., & Cuillandre, J. 2004, *PASP*, 116, 449
- Manfroid, J. 1996, *A&AS*, 118, 391
- Nugent, P., Kim, A., & Perlmutter, S. 2002, *PASP*, 114, 803
- Padmanabhan, N. et al. 2008, *ApJ*, 674, 1217
- Regnault, N. et al. 2009, *A&A*, 506, 999
- Stubbs, C. W., Doherty, P., Cramer, C., Narayan, G., Brown, Y. J., Lykke, K. R., Woodward, J. T., & Tonry, J. L. 2010, *ApJS*, 191, 376
- Stubbs, C. W. et al. 2007a, *PASP*, 119, 1163
- Stubbs, C. W. et al. 2007b, in *Astronomical Society of the Pacific Conference Series*, Vol. 364, The Future of Photometric, Spectrophotometric and Polarimetric Standardization, ed. C. Sterken, 373–+
- Vanden Berk, D. E. et al. 2001, *AJ*, 122, 549

A. Filter Set

Figure 19 illustrates the baseline LSST filter bandpasses, including a ‘standard’ atmosphere, and baseline estimates for the mirrors, lenses, filter and detector transmission and sensitivity functions.

B. Areas for further investigation

LSST is pushing to improve traditional photometric accuracy by a factor of 2, through the use of independent measurements of the hardware and atmospheric transmission curve normalization and shape. As this has never been attempted before at this level, there are understandably many areas which require further development and investigation. This section is intended to document some of those areas.

- Hardware response curve - $\phi_b^{sys}(\lambda, t)$. There is a narrow-band dome screen projector system installed at Pan-STARRS which would be extremely useful to study for comparison to the planned LSST dome screen. The PS system has demonstrated that ghosting is a significant problem in the narrow-band flat fields; it will be extremely interesting to follow how this ghosting problem is resolved. Some methods for measuring the ghosts in the PS system as a function of wavelength have already been implemented (Chris Stubbs, private communication), and these tests will feed back to the plans for the LSST dome screen projectors. ZEMAX modeling of these updated projector screens with expected LSST optical components to study ghosting and how well we can predict ghosting will be important, as well as studying how the error induced by these ghosts propagates through the rest of calibration.
- Atmospheric absorption - $\phi_b^{atm}(\lambda, t)$. Further observing runs where spectroscopic (and preferably, also broad-band photometry) observations of known sources under a variety of weather conditions and at a variety of pointings over the sky will be obtained to verify that the range of atmospheric conditions described in Section 4.2.2 are appropriate and that the model used to describe the water vapor variation across the sky is adequate. This is particularly important when considering y band photometric calibration.
- Cloud extinction. The expected cloud structure function at Cerro Pachón is not well understood; the extent of its ‘clumpiness’ as a function of total cloud extinction is a significant unknown in the self-calibration procedure. LSST plans to install small wide-field camera systems to measure cloud extinction across the sky and on small scales on Cerro Pachon to address this issue.

- Self-calibration. The self-calibration software must be developed further to run efficiently on full LSST data sets. Work is already underway to test alternative solver methods (conjugate gradient, least-squares) and add multi-threading to the solver. The extent to which additional terms can be added to the model magnitude with each of these algorithms will also be investigated. In addition, further tests to probe the boundaries of ‘where self-calibration breaks down’ will be conducted for each parameter and updated as the algorithms are improved.
- Effects on non-main sequence stars. Each of the calibration steps above have been considered in terms of main sequence stars (as these become the ‘calibration’ stars for self-calibration). However, the results of variation in the water vapor, for example, are much different for MLT dwarfs with many lines in and near the y band than for warmer main sequence stars with fewer lines. Measuring the atmospheric water vapor component to 30% may not be sufficient to meet SRD values for these sources, if the underlying SED is not well known (although see Section C). Further modeling is required to understand the full photometric calibration potential for all types of objects.

C. Photometric measurements for non-main sequence stars

LSST will record a series of m_b^{nat} measurements for each astronomical object in each visit. These m_b^{nat} measurements are generated directly from the counts recorded in each image, corrected with the photometrically uniform, broad-band flat field and for gray (cloud) atmospheric extinction effects. However, these m_b^{nat} measurements will vary as the shape of the bandpass changes, whether as a function of position in the focal plane or as a function of changes in atmospheric absorption components. Correcting for these effects requires assuming a particular SED for each source, and produces m_b^{std} values after applying Δm_b^{meas} offsets (see the overview of calibration in section 3.2 for a review).

For most objects, LSST will simply assume the source has a flat SED, which means that m_b^{std} is exactly equal to m_b^{nat} , as by definition then Δm_b^{meas} is zero. To permit scientists to generate higher precision photometry for objects using arbitrary SEDs, LSST must provide a record of $\phi_b^{meas}(\lambda, alt, az, x, y, t)$ as well as the normalization zeropoint offsets for each observation. With these additional pieces of information, scientists can generate more appropriate Δm_b^{meas} corrections, using their own chosen object SED to generate m_b^{std} . Sections 4.2.1 and 4.2.2 outline the typical magnitudes of these corrections for main sequence stars; Δm_b^{meas} can easily be on the order of 20 mmag for gri , or even 100 mmag in u band. For more extreme SEDs, these corrections may be even larger.

Figure 20 illustrates the likely magnitude of these Δm_b^{meas} corrections for a wide variety of SEDs. In each plot, the main sequence stars are shown as in the figures in the main paper (small dots, color-coded by metallicity), although given the increased scale here they only appear as a purple series of circles. M dwarfs are now included, generally mimicking the behavior of the main sequence stars but extending further into the red. More unusual SEDs are also included; a quasar SED, based on a composite of many empirical quasars from SDSS from Vanden Berk et al. (2001) that has been extended to the full LSST wavelength range through the addition of power law flux above and below the original range ($f_\nu \propto 1/\lambda^{0.5}$ for $\lambda < 89\text{nm}$ & $f_\nu \propto 1/\lambda^{1.5}$ for $\lambda > 800\text{nm}$), and redshifted from $z = 0$ to $z = 3$; also a sample of SN Ia from templates generated by Peter Nugent (Nugent et al. 2002), redshifted from $z = 0$ to $z = 1$.

The figure shows the Δm_b^{meas} values that would be expected under a maximum change of atmospheric parameters and under a likely bandpass shift. This demonstrates how much the reported m_b^{nat} values could vary for each object. If LSST was to just calculate an offset between m_b^{nat} and m_b^{std} based on an object’s color (and assuming that the object had an SED similar to a main sequence star), the resulting m_b^{std} values would be incorrect by the value of the offset between the true Δm_b^{meas} for the SED and the main sequence Δm_b^{meas} values at each color; this could easily be more than 20mmag.

With the wide variety of objects and SEDs that will be possible in the LSST data set, it is crucial to provide the information and tools so that scientists may calculate highly precise m_b^{std} magnitudes for their objects of interest. This means recording or providing the means to recalculate $\phi_b^{sys+atm}(\lambda, t)$ for every object detected with LSST.

D. Glossary

- **Level 1 Data Product.** A data product, such as a measurement of an astronomical object’s position or flux in a single image, that is computed on a nightly basis. Level 1 data products primarily consist of alerts on transient, variable and moving objects. The photometric calibration process outlined in this paper does not apply to Level 1 data products. Level 1 data products will be calibrated using all applicable prior knowledge (including secondary standard catalogs generated from previous Data Release calibration of all LSST-observed stars in the field).
- **Level 2 Data Product.** A data product, such a measurement of an astronomical object’s position or flux in either a single image or a series of images, that is computed on the Data Release schedule, on a six-month or yearly schedule. Level 2 data products

leverage all previous observations of the same object, as well as all knowledge of the LSST system accumulated to that point. The photometric calibration process outlined in this paper is used to generate Level 2 data products.

- **Normalized system response,** $\phi_b(\lambda)$. The normalized system response describes the shape of the bandpass transmission curve, separating this from the normalization of the throughput curve which can be determined separately. $\phi_b(\lambda)$ is described by Equation 5. The integral of $\phi_b(\lambda)$ is always 1.
- **Broadband flat field.** An image obtained by observing a light source which generates photons with a wide range of wavelengths (as opposed to a narrow-band flat), with relatively uniform illumination across the field of view. Night sky flats, twilight flats, and white-light or broadband dome screen flats would all generate broadband flat fields.
- **Narrow-band flat field.** An image obtained by observing a light source which generates photons with a very narrow range of wavelengths (hypothetically, even a single wavelength), with relatively uniform illumination across the field of view. A dome screen illuminated with a narrow-band laser light source will generate a narrow-band flat field.
- **‘Observed’ flat field.** A flat field, as obtained by observing the dome screen projectors. Generally would refer to a broadband flat field.
- **Photometric flat field.** A flat field which produces uniform photometric measurements across the field of view for a flat $F_\nu(\lambda)$ source. A photometric flat field must be based on a broadband flat.
- **Illumination Correction.** The ratio between the photometric flat field and the observed flat field.

$$\text{Flat}_{\text{photometric}} = \text{Flat}_{\text{observed}} * \text{IlluminationCorrection} \quad (\text{D1})$$

- **Camera Calibration Optical Bench (CCOB).** The CCOB provides a method to calibrate the spatial and wavelength-dependent response of the focal plane, unmounted from the telescope, using a well controlled, wavelength-variable, light source calibrated using a NIST photodiode. This light source, which produces a spot in the focal plane approximately the size of or smaller than the PSF, will be scanned across the detector (x, y) at a variety of beam incident angles, (θ, ϕ) and at a variety of wavelengths (λ). The response of the detector will be measured in two different configurations: one with

only the detector and the dewar window - which doubles as lens 3 (L3) - and one with the detector, L3, L2, L1, the filters and the camera shutter. The CCOB provides test data about the camera assembly for camera acceptance and to constrain the optical ZEMAX model. More details about the requirements and physical apparatus of the CCOB are available in LSST-10015 and LSST-8217.

- **Natural magnitude.** A magnitude measurement which relates directly to the number of counts measurement in an image (after including a photometric flat field correction and a rough zeropoint for an entire image). The natural magnitude relate to an ADU count that does *not* account for the color or SED of the source being observed, thus does not include any wavelength-dependent corrections. For a non-variable source observed under variable atmospheric transmission conditions and/or at varying locations in the field of view, the natural magnitude reported will change due to changes in the bandpass shape. The natural magnitude is equivalent to an observed magnitude, after the appropriate zeropoints have been applied.
- **Standard magnitude.** A magnitude measurement which includes not only corrections for the photometric flat field and a rough zeropoint for the image, but also includes a correction for wavelength-dependent effects. This means the Δm_b^{meas} appropriate to correct the natural magnitude of the object from the observed bandpass shape, $\phi_b^{meas}(\lambda, t)$, to the standard bandpass shape, $\phi_b^{std}(\lambda)$, has been calculated for the SED of the object and applied. For a non-variable source, m_b^{std} will be constant over time even if the atmospheric absorption curve or the location in the field of view changes.
- **Operations Simulation.** The Operations Simulation is a simulated pointing history of LSST, covering the sky in the same manner as the telescope could, in practice. It uses weather conditions based on historical records from Cerro Tololo, including appropriate seeing and sky brightness variations. The motion of the telescope is simulated in high fidelity, including acceleration from field to field and cable wrap. A variety of proposals are used to determine which fields to observe at each time; these proposal include the ‘universal cadence’ (satisfying most of LSST’s science requirements) and ‘deep drilling’ (a limited set of fields, observed frequently and deeply over the lifetime of the survey).

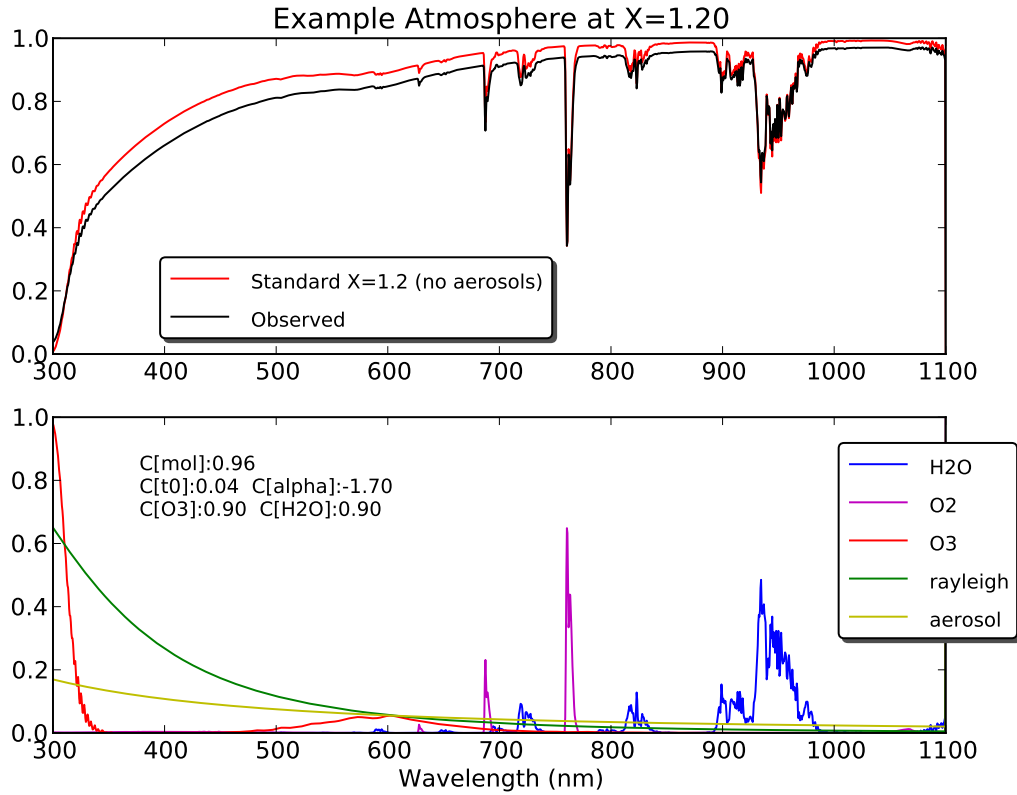


Fig. 12.—: **Example of an atmosphere generated from a typical mix of atmospheric components.** The bottom panel shows the MODTRAN absorption templates at this airmass used in generating the final atmosphere (the $A_{rayleigh}/O_2/O_3/H_2O$ and $A_{aerosol} = 1 - e^{\tau_{aerosol}}$ from Equation 25). The top panel shows the final combined atmospheric transmission curve in black, as well as a ‘standardized’ atmospheric transmission curve in red. This demonstrates that (even without using the full MODTRAN software, just the transmission templates) that we can closely recreate any atmosphere desired with any composition.

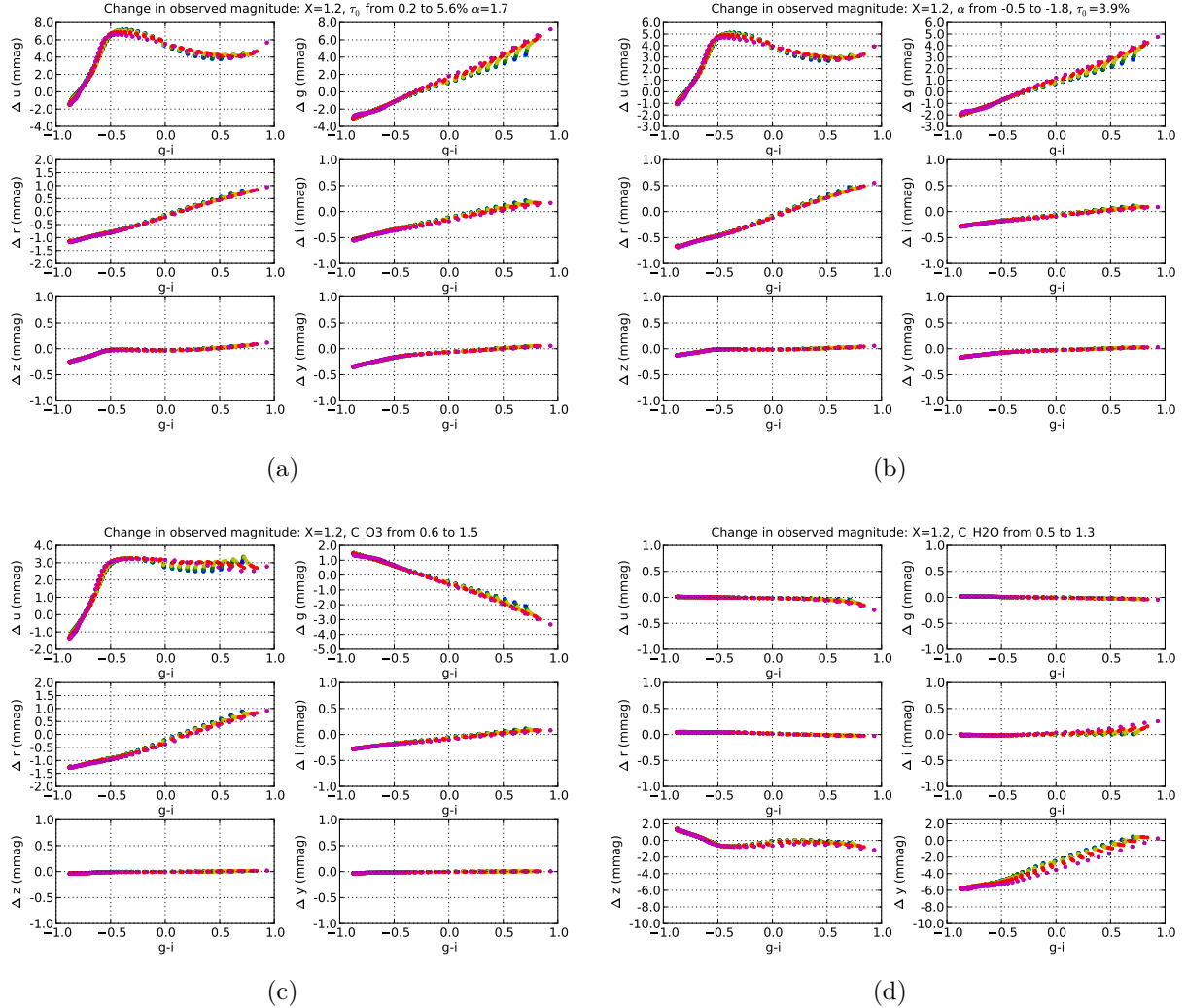
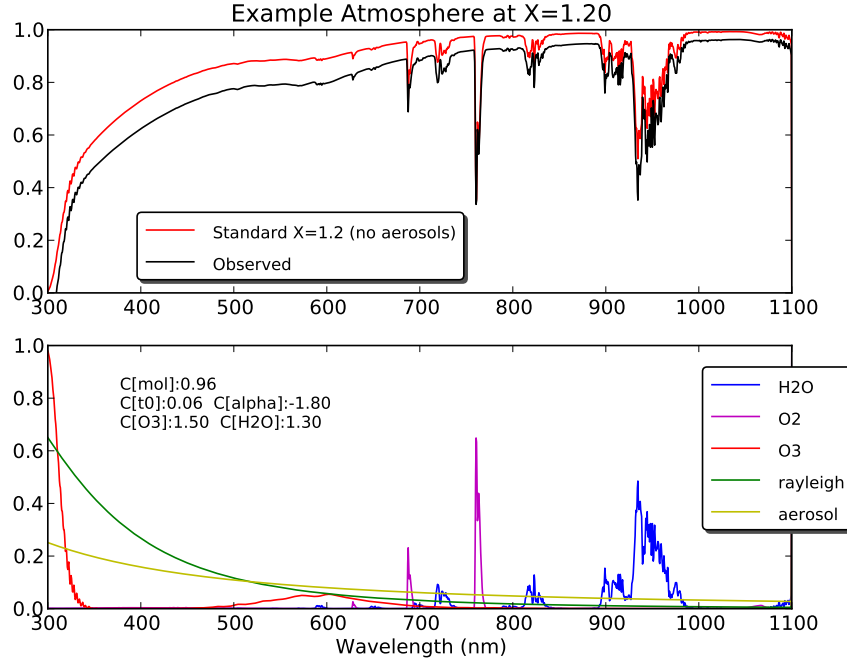
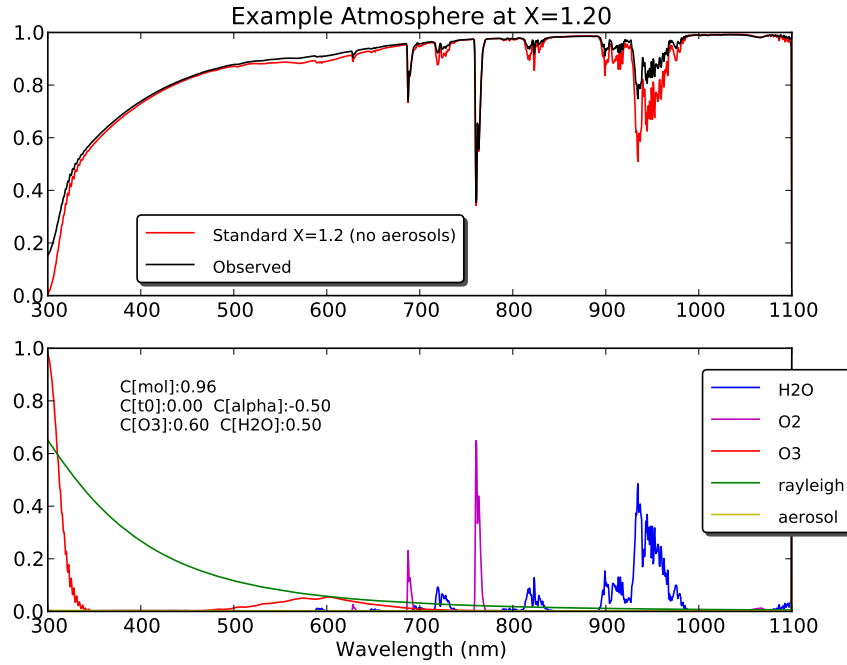


Fig. 13.—: Δm_b^{obs} due to variations of each individual absorption component. Each atmospheric transmission curve (at $X=1.2$) was combined with the set of main sequence Kurucz curves to determine the resulting changes in observed magnitudes, as in Figure 9. 13a and 13b show the effects of varying aerosol absorption in τ_0 and α respectively, 13c shows the effect of varying O₃ absorption. These effects are concentrated in u and g bands, with a negligible effect in izy . 13d shows the effect of varying the H₂O absorption, which is strongest in y , with some effect in z and no effect in $ugri$.



(a)



(b)

Fig. 14.—: ‘Extreme’ atmospheres generated from MODTRAN profiles and extremes of atmospheric coefficients. Using the extremes of $C_{\text{H}_2\text{O}}$, C_{O_3} , and τ_0 and α from Burke et al. (2010), two test atmospheres with $X = 1.2$ were created using Equation 25.

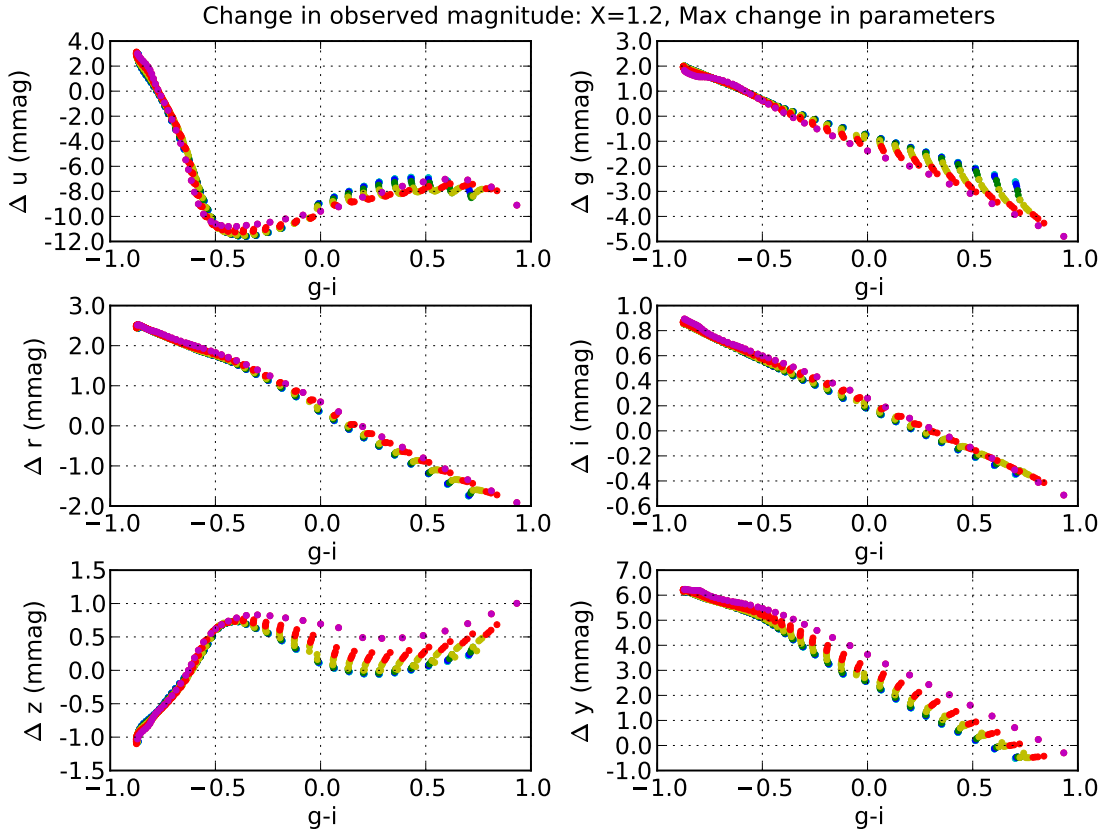


Fig. 15.—: Δm_b^{obs} due to ‘extreme’ variations of atmospheric transmission. Two atmospheric transmission curves were created using Equation 25 and the widest variations of atmospheric extinction coefficients from Burke et al. (2010). The wavelength profile of these atmospheres is shown in Figure 14. These atmospheric transmission curves were combined with the baseline LSST hardware transmission curves, and used to generate magnitudes for 850 Kurucz models with temperatures between 5000 K and 35000 K and metallicities between -5.0 and 1.0 (solar). The resulting differences in natural magnitudes between the two extremes of the atmospheric transmission in each filter are shown above.

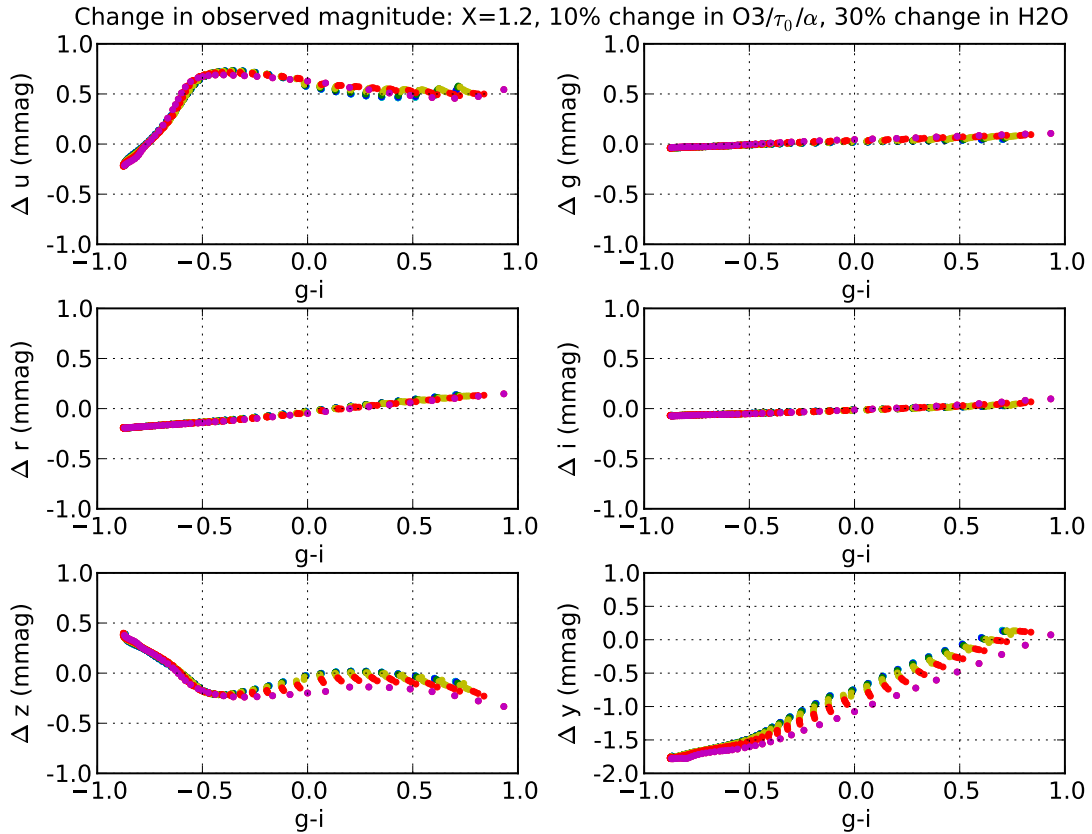


Fig. 16.—: Δm_b^{obs} due to 10% variations of atmospheric transmission in O_3 and aerosol, with 30% variation of H_2O . This is similar to Figure 15, except C_{O_3} , τ_0 and α were only varied by 10% of the total range of values measured in Burke et al. (2010), and C_{H_2O} was varied by 30% of the total range.

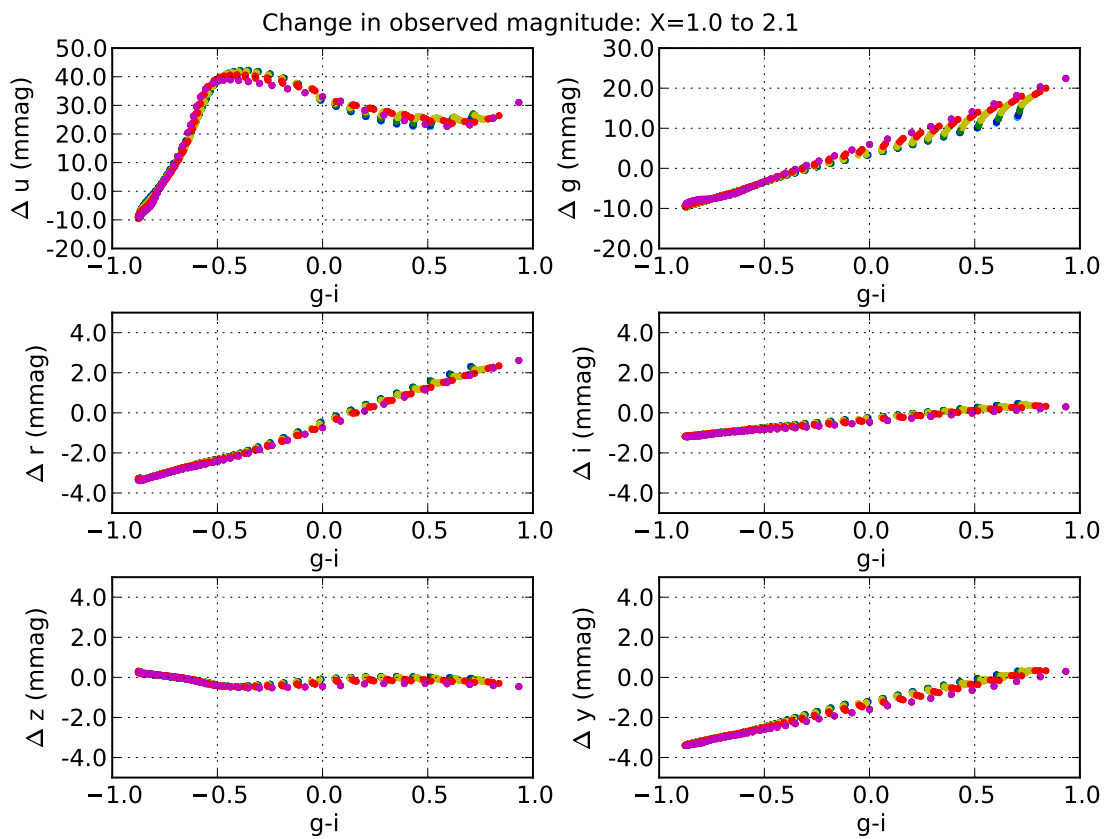


Fig. 17.—: Δm_b^{obs} due to changes in airmass from $X = 1.0$ to $X = 2.1$, for a typical atmospheric transmission response curve.

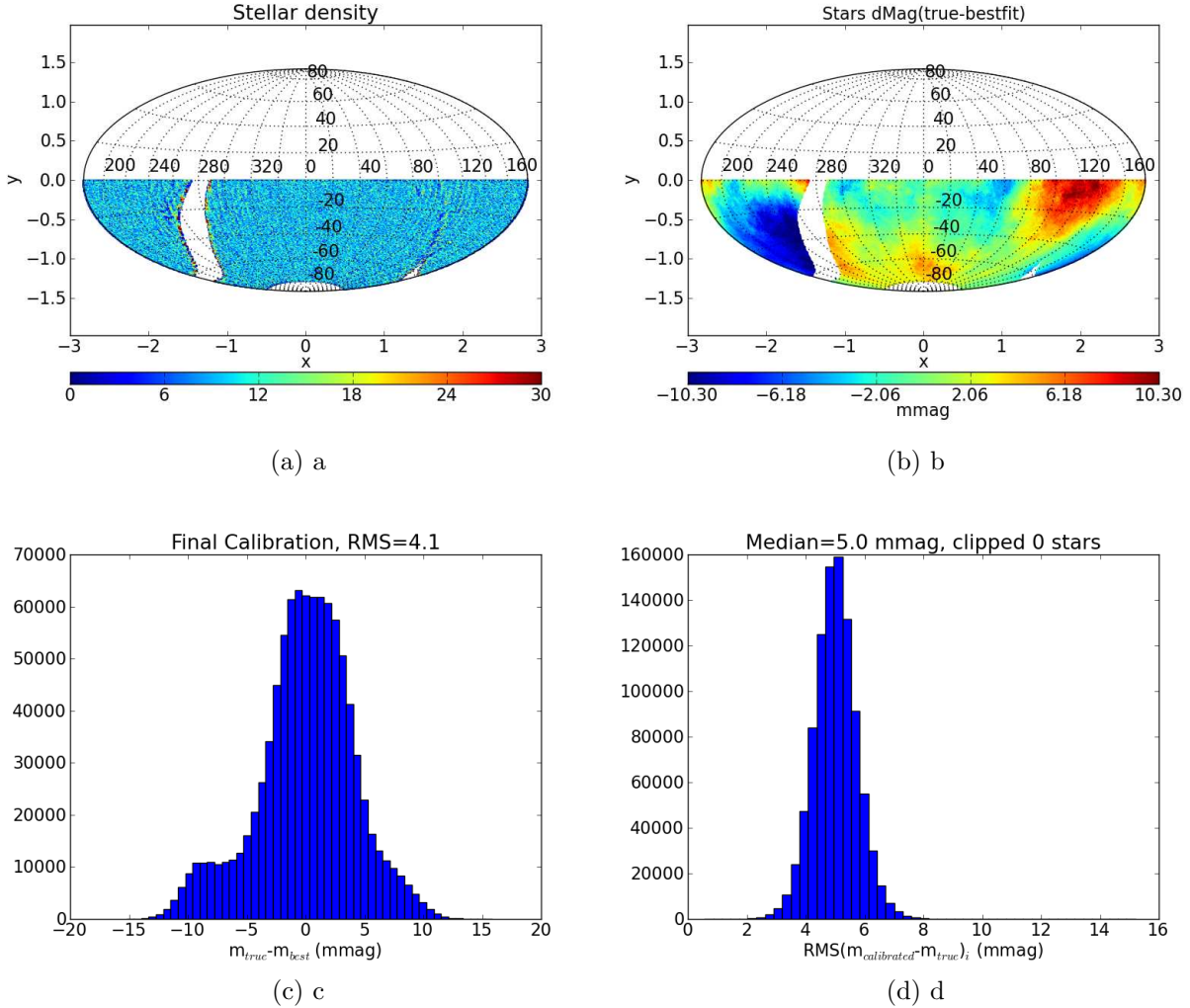


Fig. 18.—: **Results from a self-calibration investigation.** Panel (a) shows the stellar density across the sky relevant for the simulation - note the Milky Way plane has been cut out of the simulation, and we have only used pointings with declination between -80 and 0 degrees. Conditions for this simulation are described in the text. Panel (b) shows the true minus best-fit stellar magnitudes residuals across the sky after iterating the self-calibration solver. Panel (c) shows similar information, but as a histogram of all stars, demonstrating the ‘uniformity’ requirement in the SRD. Panel (d) shows a histogram of the RMS of the difference between the calibrated and true magnitudes for each star (after self-calibration iteration), demonstrating the ‘repeatability’ requirement in the SRD.

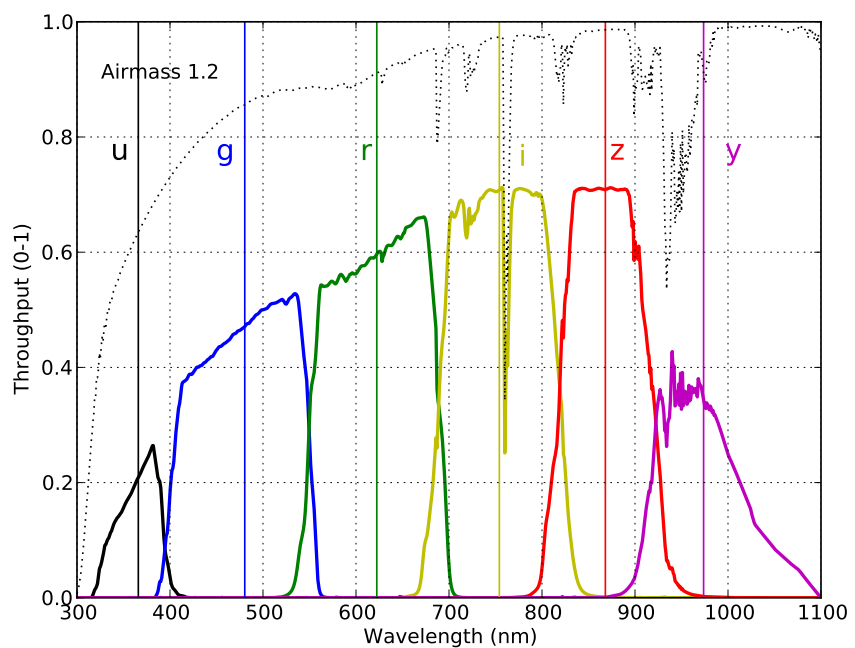


Fig. 19.—: The baseline LSST filter set.

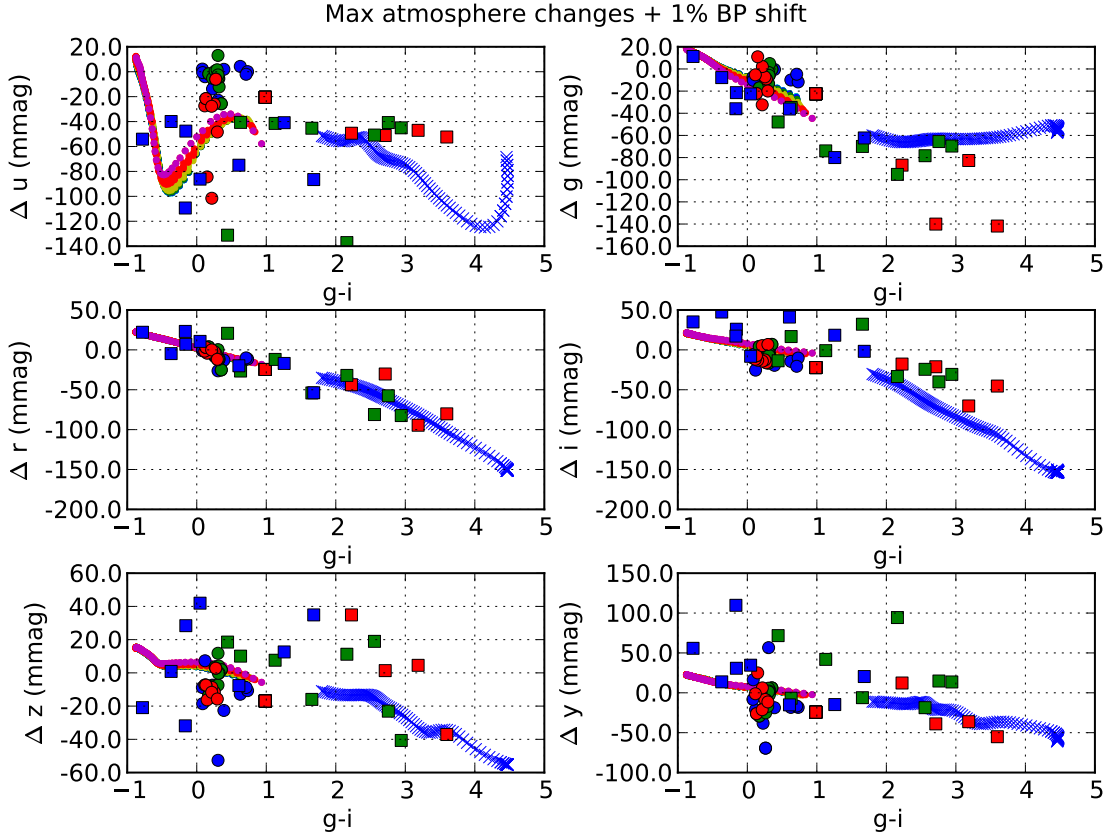


Fig. 20.—: Δm_b^{obs} due to changes in a hardware bandpass shift and a maximum change in atmospheric absorption components. This plot is similar in nature to a combination of Figure 9 and 15, but has been extended to include a wider variety of object SEDs. Main sequence stars are shown as the sequence of purple dots, and Mdwarfs are shown as the sequence of blue 'x's. The large round circles represent a quasar SED at various redshifts, color-coded with redshift as follows: $0 < z < 1$ is blue, $1 < z < 2$ is green, and $2 < z < 3$ is red. The large filled squares show the change in natural magnitudes for SNIa templates at times of 0, 20, and 40 days from peak; $0 < z < 0.36$ are blue squares, $0.36 < z < 0.72$ are green squares, and $0.72 < z < 1$ SNIa are red squares.